APPLYING MACHINE LEARNING TO OPTIMIZE SINTERED POWDER MICROSTRUCTURES FROM PHASE FIELD MODELING

by

Arunabha Batabyal

A Thesis

Submitted to the Faculty of Purdue University

In Partial Fulfillment of the Requirements for the degree of

Master of Science in Mechanical Engineering

Department of Mechanical and Energy Engineering at IUPUI

Indianapolis, Indiana

December 2020

THE PURDUE UNIVERSITY GRADUATE SCHOOL
STATEMENT OF COMMITTEE APPROVAL

Dr. Jing Zhang, Chair

Department of Mechanical and Energy Engineering

Dr. Shengfeng Yang

Department of Mechanical and Energy Engineering

Dr. Xiaoping Du

Department of Mechanical and Energy Engineering

Approved by:

Dr. Jie Chen

ACKNOWLEDGMENTS

I would like to express my sincere gratitude to my advisor, Dr. Jing Zhang for his guidance and motivation these two years that helped me accomplish this project. His encouragement to pursue the direction that I want with entire freedom has been incredible and inspired me to reach my goal. Working with him, I have also developed professionally and continue to be driven for further research in the future. I would also like to thank the members of my committee, Dr. Xiaoping Du and Dr. Shengfeng Yang, whose classes taught me invaluable lessons and concepts that helped me with this thesis work.

I would also like to thank my laboratory fellows who have extended their help whenever required. A special thanks to Homero Valladares for his sharing of knowledge regarding Bayesian Optimization. Finally, I would like to mention that the resources and infrastructure provided by the Purdue School of Engineering and Technology were an invaluable contribution towards the completion of my thesis.

TABLE OF CONTENTS

LIST OF TABLES

LIST OF FIGURES

ABSTRACT

Sintering is a primary particulate manufacturing technology to provide densification and strength for ceramics and many metals. A persistent problem in this manufacturing technology has been to maintain the quality of the manufactured parts. This can be attributed to the various sources of uncertainty present during the manufacturing process. In this work, a two-particle phase-field model has been analyzed which simulates microstructure evolution during the solid-state sintering process. The sources of uncertainty have been considered as the two input parameters surface diffusivity and inter-particle distance. The response quantity of interest (QOI) has been selected as the size of the neck region that develops between the two particles. Two different cases with equal and unequal sized particles were studied. It was observed that the neck size increased with increasing surface diffusivity and decreased with increasing inter-particle distance irrespective of particle size. Sensitivity analysis found that the inter-particle distance has more influence on variation in neck size than that of surface diffusivity. The machine-learning algorithm Gaussian Process Regression was used to create the surrogate model of the QOI. Bayesian Optimization method was used to find optimal values of the input parameters. For equal-sized particles, optimization using Probability of Improvement provided optimal values of surface diffusivity and inter-particle distance as 23.8268 and 40.0001, respectively. The Expected Improvement as an acquisition function gave optimal values 23.9874 and 40.7428, respectively. For unequal sized particles, optimal design values from Probability of Improvement were 23.9700 and 33.3005 for surface diffusivity and inter-particle distance, respectively, while those from Expected Improvement were 23.9893 and 33.9627. The optimization results from the two different acquisition functions seemed to be in good agreement with each other. The results also validated the fact that surface diffusivity should be higher and inter-particle distance should be lower for achieving larger neck size and better mechanical properties of the material.

1. INTRODUCTION

1.1 Powder Sintering

Sintering is a process of forming a solid mass of material from a powder by application of an external agent such as heat, temperature or pressure. This usually takes place below the melting temperature of the material. The sintering kinetics is characterized by multiple diffusion paths, particle rigid-body motion and grain-growth through boundary migration [1]. Sintering can also be used as heat treatment in order to increase the strength and integrity of a material. This material processing technique is very useful for custom shaping of materials which have high melting points. Materials can be produced with uniform porosity and preserved purity. Efficient control of evolving morphologies like inter-particle neck region and grain boundary is necessary for better mechanical and thermal properties and an optimized manufacturing process.

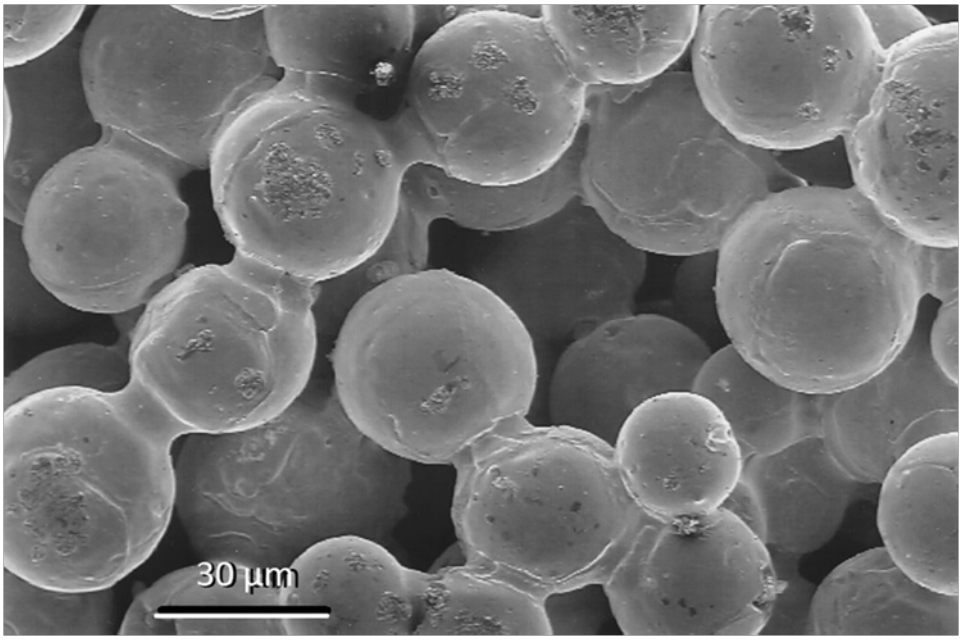

Figure 1: Scanning electron micrograph of spherical bronze particles to illustrate sinter neck formation between contacting particles prior to significant densification [2]

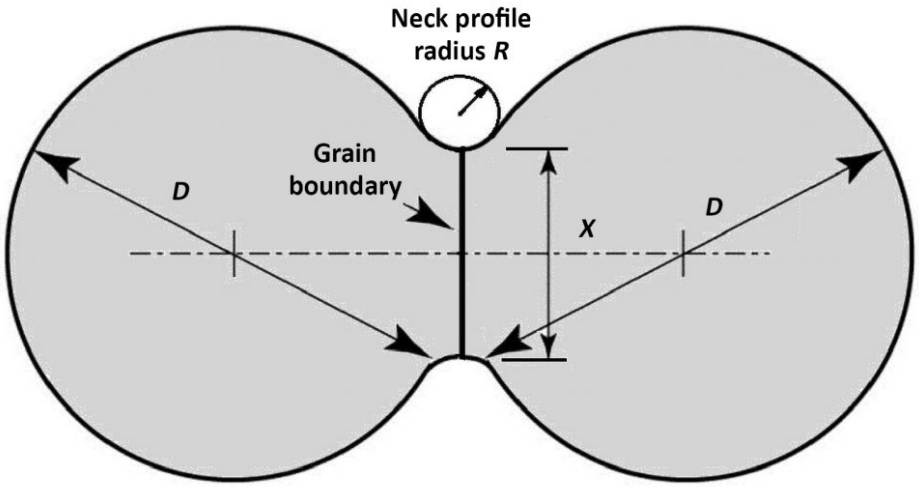

Figure 2: Outline of the neck size X and the particle size D (assumed spherical) and neck saddle point curvature R during two-particle sintering. A grain boundary forms in the neck due to crystal misalignment of the contacting particles [2]

In the current work, microstructure evolution has been studied during solid-state sintering process. During solid-state sintering, morphologies such as densification and grain growth occur. The proper control of these structural evolutions is necessary for better mechanical properties of the material. Sintering takes place due to diffusion of atoms through the microstructure of the material. The diffusion results due to a gradient in chemical potential i.e., atoms move from a region of higher chemical potential to that of a lower chemical potential. Diffusion takes place by several mechanisms like surface diffusion, vapor transport, lattice diffusion from surface, lattice diffusion from grain boundary, grain boundary diffusion, plastic diffusion, etc. Higher densification is preferred to reduce porosity in the material and smaller grain growth is desired. The microstructure evolution is driven by a reduction of total system free energy through diffusion and structural relaxation [1]. The particle rigid-body motion that occurs during sintering is driven by the diffusion of atoms from grain boundaries to nearby growing neck surface and thus leads to formation of neck region between two particles. Analysis of the simulation models has found an expression for the rate of change of neck size ratio as a function of sintering time:

$$\left(\frac{X}{D}\right)^{n} = Kt$$

Eq. 1.1

where X refers to the neck width and D the diameter of the particle. K is related to material properties and geometric assumptions. Due to the growing bonds between the grains, sintering provides strength which can be formulated as [3]:

$$\sigma_B = \Sigma V_s \frac{N_c}{\pi} \left(\frac{X}{D}\right)^2$$

Eq. 1.2

where σ_B refers to bulk sintering strength, V_s solid volumetric fractional density, N_c the packing coordination, $\frac{X}{D}$ is the neck size to particle size ratio. In sintered porous structures, the initial sintering strength varies with the square of the neck size as follows [3]:

$$\sigma_s = \frac{\sigma_0}{K} V_s \frac{N_c}{\pi} \left(\frac{X}{D}\right)^2$$

Eq. 1.3

where σ_0 refers to inherent material strength at the test temperature and K is the stress concentration factor associated with the sharp neck radius.

In the present study, the neck size has been considered the Quantity of Interest (QOI). The objective has been to control the varying neck size by designing input parameters like surface diffusivity and inter-particle distance at two different types of particle size ratios $\left(\frac{R_2}{R_1}\right)$, 1 and 1.5 where R_1 and R_2 refer to the particle radii. Henceforth, the aim has been to maximize the neck size in each case to improve the mechanical strength and integrity of the material. This in turn optimizes the manufacturing process with informed choices during the design phase.

1.2 Quality Control of Powder Sintering

However, one persistent concern in this material processing methodology as in other manufacturing technologies has been to produce parts with desired properties. Even if the same parameters are used during the manufacturing process of a specific product, it is not possible to acquire uniform properties. Pavan et al. used X-ray Computed Tomography (CT) based approach to study the effect of features' size and printing orientation on the porosity and shape deviation of each feature in Laser Sintering for polymers processing [4]. Several replicas of the test object

were made for polyamide-12 to analyze the reproducibility of the manufacturing process. It was observed that porosity levels of small features depend on their size and orientation with a smooth increase in voids' content with increased size. Also features oriented along printing direction showed an overall higher porosity value with bigger average pore sizes independent of the size of the feature. Dotchev et al. investigated polyamide 12 (PA12) powder properties deterioration in Laser Sintering process by artificially aging new and recycled grades of PA2200 powder in a temperature-controlled oven and tested using melt flow rate (MFR) indexer [5]. It was found that the powder exposed at a higher temperature and longer time experienced a higher deterioration rate. Also, powder located at the periphery and top of the build is less deteriorated than that at the center or the bottom of a long build. Karapatis et al. tried to find out to what extent the density of thin powder layers can be increased for controlling the quality of Selective Laser Sintered parts [6]. Experiments showed that the density of thin layers increased from 53% to 63% when 30% fine powder was added to coarse powder with a coarse-to-fine ratio of 1:10. However, this density improvement method was found to be less efficient as the particle do not arrange as efficiently. Yamazaki et al. studied the control mechanism of Plasma activated sintering (PAS) process and provided results for experimental conditions, instrumentation and process modeling aspects of this method along with microstructural characteristics [7]. Zarringhalam et al. showed that differential scanning calorimetry (DSC) has a good potential for quality control of Selective laser-sintered (SLS) parts [8]. DSC analysis of SLS Nylon-12 parts showed the presence of two distinct melt peaks which correspond to the melted and un-melted regions of the part. Also, it was proved that the amount of energy input during the process affects the degree of melting. Phillips et al. provided an approach of controlling temperature non-uniformity in Selective Laser Sintering (SLS) process through a feed-forward control system [9]. It was evident that a 45% improvement in ultimate flexural strength standard deviation was achieved. Kuang et al. suggested methods for controlling the sintering temperature in ceramic sintering [10]. Ultrafine grinding and grinding aids can improve the grindability, reduced the ground particle size, prevent the re-agglomeration of particles so that sintering temperature could be reduced. For ceramic powders made from wet-chemical method, co-precipitation and hydrothermal processes were suggested for production of nano-size and agglomeration-free ceramic precursor particles. Simchi et al. studied the possibility of using electrical conductivity as a tool for describing the microstructure of sintered iron compacts [11]. It was determined that the conductivity of pressed

compacts increased during the dewaxing temperature stage, the effect of sintering parameters at a higher temperature being less visible. It was established that the mechanical properties of the material can be predicted by using conductivity thus helping in quality control. Wegner et al. integrated a thermal imaging system in a laser sintering machine [12] for process monitoring. Results found that thermal imaging is well-suited for checking on powder bed surface temperature distribution and the melt's temperature. Olakanmi et al. investigated the effect of mixing time on SLS processed density and microstructure [13]. The optimal mixing time was found to be ten minutes above which the density of sintered parts decreased and hence porosity increased. This led to the deterioration of the microstructure of the SLS sintered parts. Olakanmi et al. showed that microstructural evolution in laser sintered Al-12Si powder was controlled by specific laser energy input [14]. Zhang et al. explored the densification mechanism and microstructural evolution during spark plasma sintering of boron carbide powders under a temperature range of 1700 to 2100 degree centigrade [15]. Results found that creep deformation controlled by grain-boundary sliding contributed to the densification mechanism at low-effective stress regime. At temperature higher than 2000 or at high-stress regime, the dominant mechanism was dislocation climb. Chen et al. studied the effects of mechanical milling on morphology, phase, size distribution, specific surface area of indium-gallium-zinc oxide (IGZO) [16]. It showed that the IGZO mixture particles were refined and the size difference between particles significantly decreased after milling for 45 h. Zhang et al. characterized the microstructure morphology of highly transparent yttria ceramics at low-temperature sintering [17]. Full densification could be achieved at 1450 degree centigrade for 4 h (by vacuum pre-sintering) and 1400 degree C for 3 h (by post hot isostatic pressing). The fabricated ceramics had a uniform and fine microstructure with high optical performance. Dong et al. explored the microstructural evolution and sintering kinetics during spark plasma sintering of pure tantalum powder [18]. The results found the rapid densification temperature range as 800-1300 degree C and the maximum shrinkage rate as 1100 degree centigrade. The density and grain size of the sample increased when the sintering temperature increased from 1500 to 1700 degree centigrade, the tensile strength and flexural strength also increased.

1.3 Phase-field Method for Powder Sintering

The phase-field method is an effective tool for modeling of co-evolution of microstructure and physical properties at the mesoscale. The microstructure is explained by a system of continuous variables with the interfaces having a finite width over which the variables have varying values. The evolution of the microstructural morphology is described in terms of free energy of the system. Biswas et al. studied the consolidation kinetics during sintering process using a phase-field modeling approach [19]. It was observed that the initial interactions among particles were due to surface diffusion and then densification was governed by volume and grain boundary diffusion. The grain size kept increasing under pressure and stabilized later when adjacent grains touched each other. Hotzer et al. used a phase-field model based on grand potential approach to study the microstructural evolution during solid-state sintering process [20]. The neck growth rates and particle approach in a two-particle system were compared with analytic solutions for different diffusion mechanisms and a good agreement was found between the two. Densification results for a three-dimensional green body of 24897 Al2O3-grains matched well with analytic Coble model. Biswas et al. investigated the microstructural changes during solid-state sintering using a phase-field model that included rigid-body motion, elastic deformation and heat conduction [21]. The simulations showed three distinctive stages during the sintering process - neck and grain boundary formation, neck length growth and stabilization, rapid grain growth and disappearance of one of the grains. Morphology evolution was found to be contributed by radius of particles, curvature at neck location, surface energy, grain boundary energy and variation in temperature. Asp et al. presented a phase-field model of sintering and related phenomena in a two-phase system and multi-phase system using diffusion of vacancies as the mechanism for redistribution of material [22]. The solid body was characterized by a low vacancy content, the surroundings by a high vacancy content and the surface with varying vacancy content. The temporal development of particles during solid-state sintering with wetting effects was shown in the simulations. Kumar et al. modeled sintering and simultaneous concurrent grain growth of two unequal-sized particles using a phase-field method [23] . The simulation revealed to have three sub-processes: neck growth, coarsening with concurrent slow grain boundary migration and rapid grain boundary motion. The simulation results were analyzed based on thermodynamic analysis of the driving forces for different sub-processes. The slow grain boundary migration was found to be sensitive to sintering geometry. Dzepina et al. incorporated contact mechanics

algorithm into a phase-field sintering model [24]. Energy relaxation through deformation was achieved by diffusive fluxes along stress gradients and rigid body motion of the deforming particles maintained contact between the particles. The effect of applied pressure on high pressure-high temperature (HPHT) liquid phase sintering of diamond particles was investigated and changes in neck size, particle coordination and contact flattening were observed. Termuhlen et al. introduced an approach for incorporating individual particle rigid-body motion during three-dimensional phase-field sintering simulation [25]. A grouping algorithm was introduced with a cut-off radius set on each grain to calculate the particle velocity during densification. This allowed for incorporation of densification mechanisms into three-dimensional phase-field sintering model.

1.4 Machine Learning in Powder Sintering

Machine Learning involves study of computer algorithms that can learn from data. Often seen as a subset of Artificial Intelligence or Data Science, machine learning focuses on building mathematical models that can work with unseen examples or data. The models are created based on a set of observation data also called as Training Data. The major motivation behind creating machine-learning models is imparting the ability in computers to predict complex unknown situations without being explicitly programmed or instructed to do so. Machine-learning problems can be classified into three categories based on the nature of the feedback available to the system:

- Supervised learning: Training data and output data/labels are present. The goal is to formulate a hypothesis that maps the training data to the output data.
- Unsupervised Learning: Training data is present with no output data or labels. The goal is to find hidden patterns in the training input. It is useful for finding structures in a large dataset.
- Reinforcement Learning: The algorithm interacts with a dynamic environment to act in real-time in order to maximize a reward function. It is most suitable for situations like autonomous driving, robotics, game-playing against an opponent, etc.

Statistics and Mathematical Optimization delivers theories, methods and applications towards the framework for machine learning. The prime objective of the algorithm is to build a generalized model which can produce accurate predictions for a new dataset.

Traditionally, constructing a machine-learning framework required considerable domain expertise so that raw data can be used for designing a feature extractor. This is specifically useful for tasks such as classification or pattern recognition. An emerging technique called Deep Learning improves the state-of-the-art machine-learning systems by using representation-learning methods with multiple levels of representation for automatic detection or classification [26]. Traditionally, building a machine-learning framework has required very careful engineering analysis and domain expertise. Deep Learning methods diminish this requirement by leveraging combined and abstract representation-learning frameworks that can automatically extract features or patterns from the data. Swaroop et al. proposed a machine-learning based approach to predict abnormal grain growth in powdered samples prior to actual sintering [27]. The approach was found to have a potential to allow for pre-selection of appropriate powder samples with an accuracy of 82%. This way of controlling abnormal grain growth could help reduce porosity and hence enhancement of sintered material properties. Song et al. proposed a comprehensive prediction model of sinter quality based on machine learning approach [28]. Classification model of sinter quality and regression model of sinter's total iron content were established using different machine learning algorithms. Results showed that the prediction accuracy of classification model and regression model inferred by the extra tree is the best. The F1-score of the quality index classification model was found to be 0.92 and R2 of the total iron content regression model was 0.882 thus indicating good learning and generalization ability of the proposed framework. Xiao et al. applied a deep convolution neural network to detect three typical types of powder bed defects in selective laser sintering process: warpage, part shifting and short feed [29]. The method was found to have good accuracy and efficiency and was able to cope with geometrical distortion and image blurring. Liu et al. developed a machine learning approach based on Gaussian Process Regression to identify the optimized processing window for laser powder bed fusion process (LPBF) [30]. The determined optimized processing parameters made it possible to achieve previously unattainable combinations of high strength and ductility. It was found that in addition to grain structure, the sub-grain cell size and cell boundary morphology of the LPBF fabricated AlSi10Mg strongly affected the mechanical properties of the material. Zhouzhi et al. established a method for rapid evaluation of the effect of heating rate on sintering densification based on domain-adversarial neural network [31]. This allowed for prediction of densification evolution of a material which lacked master sintering curve (MSC)

from MSC data of another material. The proposed approach could provide an efficient solution to the issue of data scarcity in sintering field. Zhang et al. presented a multi-objective optimization and analysis model of the sintering process based on BP neural network [32]. Genetic algorithms combined with BP neural network reduced the learning time and increased the forecasting accuracy of the network model. The relation between factors like quality and multi-objectives was analyzed with the results being consistent with the process.

1.5 Motivation, Objectives and Structure of Thesis

The motivation of the thesis is that since neck size is directly related to the quality and strength of the sintered part, there is a need to develop a methodology to optimize the neck size. The objective of the thesis is to use machine learning approach to find out optimal values of surface diffusivity and inter-particle distance for maximizing neck size for equal and unequal sized particles.

The structure of the thesis is as follows:
Chapter 1 provides an introduction. Chapter 2 elaborates the model details and mechanisms i.e., phase-field model for simulation of neck growth in a non-contacting two-particle system, surrogate models via Machine Learning approach, sensitivity analysis and surrogate-based input parameter optimization through a Bayesian Optimization algorithm. Chapter 3 lists all the results of the models mentioned in chapter 2 and also includes discussion regarding the same. Chapter 4 concludes the thesis with major points learned from this work and also proposes some future activities that can be carried out to extend this work further.

2. NUMERICAL MODEL DETAILS

2.1 Phase-field model

In the present study, the neck formation between two non-contacting spherical particles has been focused on. The phase-field model and its codes for solid-state sintering in Ref. [33] have been adopted for the current work to generate the microstructures of the two-particle model. Two types of field variables have been used to represent the microstructure. The conserved density field ρ that assumes the value of one at the solid phase and zero at the pores, varying at the solid-pore interface. The non-conserved order parameter η_i has been used to distinguish the different particles in the microstructure. The order parameter takes the value of one for a specific particle and zero for the other particles. The value also varies from zero to one or one to zero across the grain boundaries.

2.1.1 Governing equations of phase-field model

The microstructure is defined by the free energy function of the system which is mathematically represented as:

$$F = \int_v [f(\rho, \eta 1, \dots p) + \frac{k_\rho}{2}(\nabla\rho)^2 + \sum_i \frac{k_\eta}{2}(\nabla\eta_i)^2]dv \quad \text{Eq. 2.1}$$

where k_ρ and k_η are gradient energy coefficients for concentration and grain boundary energies respectively [33]. The evolution equation for density field follows the Cahn-Hilliard equation:

$$\frac{\partial\rho}{\partial t} = \nabla.\left(\frac{D\nabla\delta\mathrm{F}}{\delta\rho}\right) = \nabla.\,\mathrm{D}\nabla\left(\frac{\partial\mathrm{f}}{\partial\rho} - k_\rho\nabla^2\rho\right) \quad \text{Eq. 2.2}$$

where D is the microstructure-dependent diffusivity coefficient [33]. D is assumed to take the form:

$$D = D_{vol}\,\phi(\rho) + D_{vap}\,[1 - \phi(\rho)] + D_{surf}\,\rho(1-\rho) + D_{GB}\sum_{i}\sum_{i\neq m}\eta_i\eta_m$$

Eq. 2.3

where D_{vol} is the bulk diffusivity, D_{vap} is the diffusivity of the vapor phase, D_{surf} is the surface diffusivity and D_{GB} is the grain boundary diffusivity. The interpolation function $\phi(\rho)$ is assumed as:

$$\phi = \rho^3(10 - 15\rho + 6\rho^2)$$

Eq. 2.4

This ensures the bulk diffusivity is zero at the pores and one at the solid regions. The non-conserved order parameter which represents the particles and the grain boundaries follows the Allen-Cahn equation:

$$\frac{\partial \eta_i}{\partial t} = -\frac{L}{\partial \eta_i}\delta F = -L\left(\frac{\partial F}{\partial \eta_i} - k_\eta \nabla^2 \eta_i\right)$$

Eq. 2.5

where *L* is the grain-boundary mobility [33].

The Cahn-Hilliard and Allen-Cahn governing equations were solved with finite difference algorithm by using five-point stencil in two-dimensional space. The time integration was carried out by simple explicit Euler time marching scheme.

2.1.2 Geometry and mesh of equal size and unequal size two-particle models

For equal-sized particles, the radii of the two spherical particles were made equal and the model was simulated for 20,000 time steps. The radius of each particle was 20 units. The simulation cell was discretized into 100 grid points in the x-direction and 100 grid points in the y-direction. The grid spacing was 0.5 in both x and y directions. The inter-particle distance was kept as 40 units initially and was varied according to the uniform distribution.

For unequal sized particles, the radius of one of the spherical particles was made 1.5 times of that of the other and the phase-field model was simulated for 20,000 time steps. The radius of one particle was 20 and that of the other was 40/3. The simulation cell was discretized into 100 grid points in the x-direction and 100 grid points in the y-direction. The grid spacing was 0.5 in both x and y-directions. The inter-particle distance varied from 33.3 through 34.8.

2.1.3 Material properties

The gradient coefficient for concentration field k_ρ was set to 5.0, the gradient coefficient for order parameters k_η was assigned value of 2.0, mobility of order parameters L set as 10.0 [33]. The value of bulk diffusivity D_{vol} was 0.04, diffusivity of the vapor phase D_{vap} 0.002, initial surface diffusivity D_{surf} 16.0, grain boundary diffusivity D_{GB} 1.6 [33]. Since the values in the phase-field model were normalized, temperature was not considered as an explicit input parameter. However, temperature effect can be included by using temperature-dependent material properties.

2.1.4 Boundary conditions

The concentration field which takes the value of 1 in the particles and 0 elsewhere was initialized to 0. It is a one-dimensional array and can be represented as $con(N_x N_y)$.. The two-dimensional array of non-conserved order parameters for the particles $etas(N_x N_y, npart)$ was initialized to 0. $N_x N_y$ represents the total number of grid points in the simulation cell and $npart$ is the number of particles.

2.2 Machine Learning Approach

2.2.1 Gaussian Process Regression

A Gaussian Process is a set of random variables, any finite number of which have joint Gaussian distributions [34]. A random variable is any variable whose value depends on the outcome of a random phenomenon. Any random variable can be described by its cumulative distribution

function which describes the probability that the random variable will be less than or equal to a certain value. The cumulative distribution function can be described as:

$$F_X(x) = P(X \leq x)$$

Eq. 2.6

where X is the random variable and x is the target value. A joint distribution is used when we want to study two random variables together. For instance, the joint cumulative distribution function of two random variables X and Y can be represented as:

$$F_{XY}(x, y) = P(X \leq x, Y \leq y)$$

Eq. 2.7

which can also be represented as:

$$F_{XY}(x, y) = P((X \leq x) \cap (Y \leq y))$$

Eq. 2.8

A Gaussian Process consists of a mean function m(x) and a covariance function k(x, x'). The Gaussian distribution can be indicated as:

$$f \sim GP(m, k)$$

Eq. 2.9

which means the function f is distributed as a Gaussian Process with mean function m and covariance function k [34]. The individual random variables in a vector from a Gaussian distribution are indexed by their position in the vector. For example, if the input variable is denoted by x, then for each input x, there is an associated random variable $f(x)$ which is the value of the stochastic function f at that location. The Gaussian Process regression function also known as Kriging has a basis function that can be formulated as [35]:

$$\psi^i = \exp\left(-\sum_{j=1}^{k} \theta_j \left| x_j^{(i)} - x_j \right|^{p_j}\right)$$

Eq. 2.10

The θ in the equation above allows the width of the basis function to vary from variable to variable [35]. The varying value of p_j allows for the smoothness to vary for the function. As

mentioned earlier, each input variable has an associated random output variable, so the observed responses can be denoted by a set of random vectors:

$$\boldsymbol{Y} = \begin{pmatrix} Y(x^1) \\ \vdots \\ Y(x^n) \end{pmatrix}$$

Eq. 2.11

The random vector has a mean of $\mathbf{1}\mu$ where $\mathbf{1}$ is an $n \times 1$ column vector of ones. The random variables are correlated with each other by the expression:

$$cor\left[Y\left(x^i\right), Y(x^l)\right] = \exp(-\sum_{j=1}^{k} \theta_j \left|x_j^i - x_j^l\right|^{p_j})$$

Eq. 2.12

From this an $n \times n$ correlation matrix can be constructed for the observed samples:

$$\boldsymbol{\Psi} = \begin{pmatrix} cor[Y(x^1), Y(x^2)] & \cdots & cor[Y(x^1), Y(x^n)] \\ \vdots & \ddots & \vdots \\ cor[Y(x^n), Y(x^1)] & \cdots & cor[(Y(x^n), Y(x^n)] \end{pmatrix}$$

Eq. 2.13

A covariance matrix can be created from the above correlation matrix [35]:

$$Cov(\boldsymbol{Y}, \boldsymbol{Y}) = \sigma^2 \boldsymbol{\Psi}$$

Eq. 2.14

Correlation refers to the degree at which two random variables are linearly related to each other. There are several correlation coefficients like Pearson correlation coefficient, Spearman's rank correlation coefficient, Kendall's rank correlation coefficient, etc. The value of the correlation coefficient can vary between -1 and +1. A value of +1 refers to a perfect linearly increasing relationship between the two variables. A value of -1 refers to a perfect linearly decreasing relationship between the variables. A value of 0 refers to no correlation or dependence between the variables. The closer the coefficient is to -1 or +1, the stronger the correlation is between the variables. Covariance is defined as the correlation between two or more sets of random variables. For two random variables X and Y,

$$Cov(X,Y) = E\left[(X-\mu_x)(Y-\mu_y)\right]$$

Eq. 2.15

$$= E[XY] - \mu_x\mu_y$$

Eq. 2.16

where μ_x and μ_y are the means of X and Y and E is the expectation. The relation between correlation and covariance can be represented as [35]:

$$cor(X,Y) = \frac{cov(X,Y)}{\sigma_x\sigma_y}$$

Eq. 2.17

The correlation between the elements of $\boldsymbol{Y}$ depends on the values of absolute distance between the sample points $\left|x_j^i - x_j^l\right|$, the parameters p_j and θ_j. It has been observed that as the two points move close together i.e., $x_j^i - x_j^l \to 0$, $\exp\left(-\left|\mathrm{x_j^i} - \mathrm{x_j^l}\right|^{\mathrm{p_j}}\right) \to 1$ i.e., the points show highly increasing linear correlation whereas when the distance$\to \infty$, the correlation coefficient$\to 0$, i.e., the points have no correlation. θ_j is a width parameter that affects how far a data point's influence extends. A low θ_j means all data points have a high correlation [35] while the reverse is true for a high θ_j. Hence θ_j can be considered as a measure of how active the approximating function is. The value of θ and p can be found out by maximizing the likelihood of the observed responses $\boldsymbol{Y}$. Taking the natural logarithm of likelihood :

$$\ln(L) = -\frac{n}{2}\ln(2\pi) - \frac{n}{2}\ln(\sigma^2) - \frac{1}{2}\ln|\boldsymbol{\Psi}| - \frac{(\boldsymbol{y}-\boldsymbol{1}\mu)^T\boldsymbol{\Psi}^{-1}(\boldsymbol{y}-\boldsymbol{1}\mu)}{2\sigma^2}$$

Eq. 2.18

The maximum likelihood estimates (MLEs) for μ and σ^2:

$$\hat{\mu} = \frac{\boldsymbol{1}^T\boldsymbol{\Psi}^{-1}\boldsymbol{y}}{\boldsymbol{1}^T\boldsymbol{\Psi}^{-1}\boldsymbol{1}}$$

Eq. 2.19

$$\hat{\sigma}^2 = \frac{(\boldsymbol{y}-\boldsymbol{1}\mu)^T\boldsymbol{\Psi}^{-1}(\boldsymbol{y}-\boldsymbol{1}\mu)}{n}$$

Eq. 2.20

The concentrated ln-likelihood function can be denoted as [35]:

$$\ln(L) \approx -\frac{n}{2}\ln(\sigma^2) - \frac{1}{2}\ln|\boldsymbol{\Psi}|$$

Eq. 2.21

The values of $\theta \; and \; p$ are found to maximize the above ln-likelihood function. This is usually done through a genetic algorithm or exhaustive search function. The maximum likelihood estimate (MLE) for the Kriging prediction $\hat{y}$ is given by [35]:

$$\hat{y}(\boldsymbol{x}) = \hat{\mu} + \boldsymbol{\psi}^T \boldsymbol{\Psi}^{-1}(\boldsymbol{y} - \mathbf{1}\hat{\mu})$$

Eq. 2.22

2.2.2 Surrogate Modeling

Surrogate models are approximations of the original simulation model. They are cheap to evaluate unlike the multi-physics simulation models. They can often be used when it is not possible to predict the outcome of a model by any other method. They consider the original simulation model as a black box and require little to no knowledge about its inner working. The Gaussian Process Regression (Kriging) methodology has been used here to build the surrogate models that predict neck size from input parameters surface diffusivity and inter-particle distance. A 4-level full factorial Design of Experiments (DOE) was performed in the process of creating the surrogate model. First, the design variables and response variables were determined. In this case, the design variables were surface diffusivity and the inter-particle distance. The response variable was certainly the size of the evolved neck region in-between the two spherical particles. The statistical design of experiments allows varying all variables simultaneously rather than varying one-factor-at-a-time [36]. This way the mutual interactions between the variables are also considered. So the quantity of interest neck size can be modeled as a function of these two design variables:

$$N = f\left(D_{surf}, d\right)$$

Eq. 2.23

where N refers to the neck size, D_{surf} stands for surface diffusivity and d refers to the inter-particle distance.

2.2.3 Training data

Table 1 and Table 2 below show the DOE matrix for equal-sized and unequal sized particles respectively. Sixteen simulations of the phase-field model were performed at varying values of the input parameters. A uniform distribution of data was considered for both surface diffusivity and inter-particle distance. For equal-sized particles, the range of surface diffusivity was [4, 24] and that for inter-particle distance [40, 41.5] while for unequal sized particles, the ranges were [4, 24] and [33.3, 34.8] respectively. There was not much difference in values of neck size at higher time steps. Hence, in order to reduce computational expense, the total time steps were kept at 5000 and the neck size after each simulation was noted. The trend in response values was found to be monotonic, so even if more simulations were performed, the additional data points would be on the same surfaces.

Table 1: DOE matrix for equal-sized particles

Serial No.	Surface diffusivity (D_{surf})	Inter-particle distance (d)	Neck size(N)
1	4	40	14.15388
2	8	40	15.50387
3	16	40	17.18751
4	24	40	19.36508
5	4	40.5	12.40309
6	8	40.5	13.95348
7	16	40.5	15.748
8	24	40.5	16.69287
9	4	41	8.00002
10	8	41	9.53848
11	16	41	12.1875
12	24	41	14.1732
13	4	41.5	5.84617
14	8	41.5	7.75193
15	16	41.5	10.39367

Table 1 continued

16	24	41.5	12.28342

Table 2: DOE matrix for unequal sized particles

Serial No.	Surface diffusivity (D_{surf})	Inter-particle distance (d)	Neck size (N)
1	4	33.3	12.093
2	8	33.3	13.2308
3	16	33.3	14.68752
4	24	33.3	15.55554
5	4	33.8	10.46155
6	8	33.8	11.47285
7	16	33.8	13.22831
8	24	33.8	14.28572
9	4	34.3	6.82169
10	8	34.3	8.37208
11	16	34.3	10.39367
12	24	34.3	12.06348
13	4	34.8	4.30771
14	8	34.8	6.76924
15	16	34.8	9.06252
16	24	34.8	10.39367

Observations 4, 5, 6 and 7 in both Table 1 and Table 2 were kept aside for model testing purpose and were not used for generating the metamodels.

2.2.4 Metamodel generation

The metamodel was generated from the training data through Gaussian Process Regression. The ooDACE toolbox was used for the creation of the surrogate model [37]. A fourth of the data in

Tables 1 and 2 were left out and kept reserved for validation and testing the accuracy of the model. The lower bound and upper bound of the hyper-parameters were fixed at [-5 5]. Three Gaussian regression functions of orders zero, one and two were tested for building the metamodel. A meshgrid of size 100×100 was created to plot the surface of neck size.

2.2.5 Model testing

For model testing purpose, the root mean squared error (RMSE) can be used as a metric [35]. If the available observed data is enough, $0.25n$ $x \rightarrow y$ pairs can reserved for model testing [38]. RMSE can be formulated as:

$$\sqrt{\frac{\sum_{i=0}^{n_t}(y^i - \hat{y}^i)^2}{n_t}} \qquad \text{Eq. 2.24}$$

where n_t is the number of observations for testing, y^i is the i^{th} observation and $\hat{y}^i$ is the prediction corresponding to the i^{th} observation [35].

Table 3: Model Testing data for equal-sized particles

Serial No.	Surface diffusivity (D_{surf})	Inter-particle distance (d)	Neck size(N)
1	24	40	19.36508
2	4	40.5	12.40309
3	8	40.5	13.95348
4	16	40.5	15.748

Table 4: Model Testing data for unequal sized particles

Serial No.	Surface diffusivity (D_{surf})	Inter-particle distance (d)	Neck size(N)
1	24	33.3	15.55554

Table 4 continued

2	4	33.8	10.46155
3	8	33.8	11.47285
4	16	33.8	13.22831

2.2.6 Cross-validation

Cross-validation is a technique to test how accurately a predictive model will perform in real life. The goal is to test the model's ability to predict new data that was not used as training data. This can help to avoid problems like overfitting or underfitting of the model and generalize the model for working on unknown datasets. Cross-validation involves partitioning the data into subsets called training set and validation set. In one round, the model is built using the training set and validated using the validation/testing set. Multiple rounds are performed like this with different subsets to reduce variability. The error in prediction is found in each round. The average error for all rounds gives an estimate of the accuracy of the predictive capability of the model. There are two types of cross-validation methods: Exhaustive and Non-exhaustive. The exhaustive methods include Leave-p-out cross-validation, Leave-one-out cross-validation, while the non-exhaustive methods include k-fold cross-validation, Holdout method, Repeated random sub-sampling validation. In this work, the Leave-one-out cross-validation (LOOCV) has been used to evaluate the surrogate model. In LOOCV, the dataset is divided into k subsets where k equals the total number of observations. The function approximator is trained on all the data except for one point and prediction is made for that point. The average error is computed from all such predictions. Though it can be a little computationally expensive, it gives accurate measure of the predictability of the machine-learning model. The advantage is that the variance is reduced to minimum and it does not depend on how the dataset is subdivided unlike other cross-validation methods. Mathematically, if a mapping $\zeta: \{1, \dots, n\} \to \{1, \dots, k\}$ describes the allocation of n training points to one of the k subsets and $\hat{f}^{-i}$ is the value of the predictor obtained by removing the subset $\zeta(i)$, the cross-validation measure can be depicted as [35]:

$$\epsilon_{CV} = \frac{1}{n}\sum_{i=1}^{n} |y^i - \hat{f}^{-i}|$$

Eq. 2.25

where the absolute error has been taken into account between the i^{th} test response and the i^{th} predicted value.

Table 5: Cross-Validation data for equal-sized particles

Serial No.	Surface diffusivity (D_{surf})	Inter-particle distance (d)	Neck size(N)
1	4	40	14.15388
2	8	40	15.50387
3	16	40	17.18751
4	24	40	19.36508
5	4	40.5	12.40309
6	8	40.5	13.95348
7	16	40.5	15.748
8	24	40.5	16.69287
9	4	41	8.00002
10	8	41	9.53848
11	16	41	12.1875
12	24	41	14.1732
13	4	41.5	5.84617
14	8	41.5	7.75193
15	16	41.5	10.39367
16	24	41.5	12.28342

Table 6: Cross-Validation data for unequal sized particles

Serial No.	Surface diffusivity (D_{surf})	Inter-particle distance (d)	Neck size (N)
1	4	33.3	12.093
2	8	33.3	13.2308
3	16	33.3	14.68752
4	24	33.3	15.55554
5	4	33.8	10.46155
6	8	33.8	11.47285
7	16	33.8	13.22831
8	24	33.8	14.28572
9	4	34.3	6.82169
10	8	34.3	8.37208
11	16	34.3	10.39367
12	24	34.3	12.06348
13	4	34.8	4.30771
14	8	34.8	6.76924
15	16	34.8	9.06252
16	24	34.8	10.39367

Each observation here was considered a subset. So for each iteration, fifteen sets of training data were available and one set of test (validation) data was present. The error was found in each iteration by subtracting the predicted response from the test response.

2.2.7 Sensitivity Analysis

Sensitivity Analysis can determine how robust the result is. It can help save time and make informed decisions or choices. Sensitivity Analysis finds out which input variable has more contribution towards the variation of the output response variable. Global Sensitivity Analysis

(GSA) takes into account all input variables in a model and determines sensitivity by evaluating over the entire range of each input variable [39].

2.2.8 Pearson product-moment correlation coefficient

The Pearson product-moment correlation coefficient can be used to determine the contribution of each input parameter on the variability of the response QOI i.e., neck size [40].

$$\text{Corr}\left(D_{surf}, N\right) = \rho_{D_{surf}\,N} = \frac{\text{Covariance}(D_{surf}, N)}{\sigma_{D_{surf}}\,\sigma_N}$$

Eq. 2.26

$$\text{Corr}(d, N) = \rho_{dN} = \frac{\text{Covariance}(d, N)}{\sigma_d \sigma_N}$$

Eq. 2.27

where D_{surf} is the surface diffusivity, d is the inter-particle distance, N the neck size, $\sigma_{D_{surf}}$, σ_d and σ_N are the standard deviations of D_{surf}, d and N respectively.

2.2.9 Bayesian Optimization

Bayesian Optimization is a class of machine-learning-based optimization methods focused on solving the problem

$$\max_{x \epsilon A} f(x)$$

Eq. 2.28

where $f(x)$ is the objective function, x is the input, A is the feasible set. The input x is in $\mathbb{R}^d$ for a value of d that is not too large, typically $d \leq 20$. The feasible set A is a hyper-rectangle $\{x \epsilon \mathbb{R}^d : a_i \leq x_i \leq b_i\}$ or the d-dimensional simplex $\{x \epsilon \mathbb{R}^d : \sum_i x_i = 1\}$. The objective function f is continuous and modeled using Gaussian Process Regression. f usually lacks any known special structure like concavity or linearity that would make it easy to optimize using techniques that leverage such structure to improve efficiency. So f is considered as a black-box. This type of optimization is also referred to as derivative-free optimization as there is no evaluation of first or second-order derivatives. Bayesian optimization consists of two main components: a Bayesian

statistical model for modeling the objective function and an acquisition function to decide where to sample next. The statistical model which is usually a Gaussian process, provides a Bayesian posterior probability distribution that describes potential values for $f(x)$ at a candidate point x. For each evaluation of f at a new point, the posterior distribution is updated. The acquisition function measures the value that would be generated by evaluation of the objective function at a new infill point x based on current posterior distribution over f. The Gaussian Process-based models permit the calculation of an estimated error in the model, hence it is possible to use this to position infill points where the uncertainty in the prediction of the model is highest. The mean squared error (MSE) in a Gaussian process-based prediction model is [35]

$$\hat{s}^2(\mathbf{x}) = \sigma^2 \left[1 - \boldsymbol{\psi}^T \boldsymbol{\Psi}^{-1} \boldsymbol{\psi} + \frac{1 - \mathbf{1}^T \boldsymbol{\Psi}^{-1} \boldsymbol{\psi}}{\mathbf{1}^T \boldsymbol{\Psi}^{-1} \mathbf{1}} \right]$$

Eq. 2.29

Using this estimated error, the uncertainty in prediction can be modeled by considering it as the realization of a normally distributed random variable $Y(\mathbf{x})$ with mean $\hat{y}(\mathbf{x})$ and variance $\hat{s}^2(\mathbf{x})$. Considering the possibility that $Y(\mathbf{x})$ can take different values, due to the size of $\hat{s}^2(\mathbf{x})$, infill criteria can be made which balances the values of $\hat{y}(\mathbf{x})$ and $\hat{s}^2(\mathbf{x})$. One way to balance these two is minimizing a statistical lower bound [35]:

$$\mathrm{LB}(\mathbf{x}) = \hat{y}(\mathbf{x}) - A\hat{s}(\mathbf{x})$$

Eq. 2.30

where A is a constant that controls the exploitation/exploration balance. As $A \to 0$, $\mathrm{LB}(\mathbf{x}) \to \hat{y}(\mathbf{x})$ (pure exploitation) and as $A \to \infty$, the effect of $\hat{y}(\mathbf{x})$ becomes negligible and minimizing $\mathrm{LB}(\mathbf{x})$ is equivalent to maximizing $\hat{s}(\mathbf{x})$ (pure exploration) [35].

2.2.10 Optimization using Probability of Improvement

Usually, the infill point is placed at a value of $\mathbf{x}$ that will help in an improvement on the best observed value so far, i.e., $y_{\min}$ [35]. By considering $\hat{y}(\mathbf{x})$ as the realization of a random variable, the probability of improvement can be calculated as $I = \frac{y_{\min} - Y(\mathbf{x})}{y_{\min}}$ [35].

$$P[I(\mathbf{x})] = \frac{1}{\hat{s}\sqrt{2\pi}} \int_{-\infty}^{0} e^{-[I-\hat{y}(\mathbf{x})]^2/(2s^2)} \mathrm{d}I$$

Eq. 2.31

Using the error function,

$$P[I(\mathbf{x})] = \frac{1}{2}\left[1 + \mathrm{erf}\left(\frac{y_{\min} - \hat{y}(\mathbf{x})}{\hat{s}\sqrt{2}}\right)\right]$$

Eq. 2.32

For a maximization problem,

$$I = \frac{Y(\mathbf{x}) - y_{\max}}{y_{\max}}$$

Eq. 2.33

2.2.11 Optimization using Expected Improvement

If the mean $\hat{y}(x)$ and the variance $\hat{s}^2(x)$ are provided, the amount of improvement over the current model can be determined. The Expected Improvement can be calculated by [35]:

$$E[I(x)] = \left(y_{min} - \hat{y}(x)\right)\Phi\left(\frac{y_{min} - \hat{y}(x)}{\hat{s}(x)}\right) + s\phi\left(\frac{y_{min} - \hat{y}(x)}{\hat{s}(x)}\right) if\ s > 0$$

Eq. 2.34

$$= 0\ if\ s = 0$$

Eq. 2.35

where $\Phi(.)$ and $\phi(.)$ are the cumulative distribution function and probability density function respectively. A maximum expected improvement infill procedure usually finds the global optimum. Using the error function, the expected improvement can be expressed as:

$$E[I(\mathbf{x})] = \left(y_{\min} - \hat{y}(\mathbf{x})\right)\left[\frac{1}{2} + \frac{1}{2}\mathrm{erf}\left(\frac{y_{\min} - \hat{y}(\mathbf{x})}{\hat{s}\sqrt{2}}\right)\right] + \hat{s}\frac{1}{\sqrt{2\pi}}\exp\left[\frac{-\left(y_{\min} - \hat{y}(\mathbf{x})\right)^2}{2\hat{s}^2}\right]$$

Eq. 2.36

Figure 3 shows a Gaussian RBF prediction for a function by finding the minimum of the RBF model. However, the search of the original function gets stuck at a local optimum instead of the global optimum.

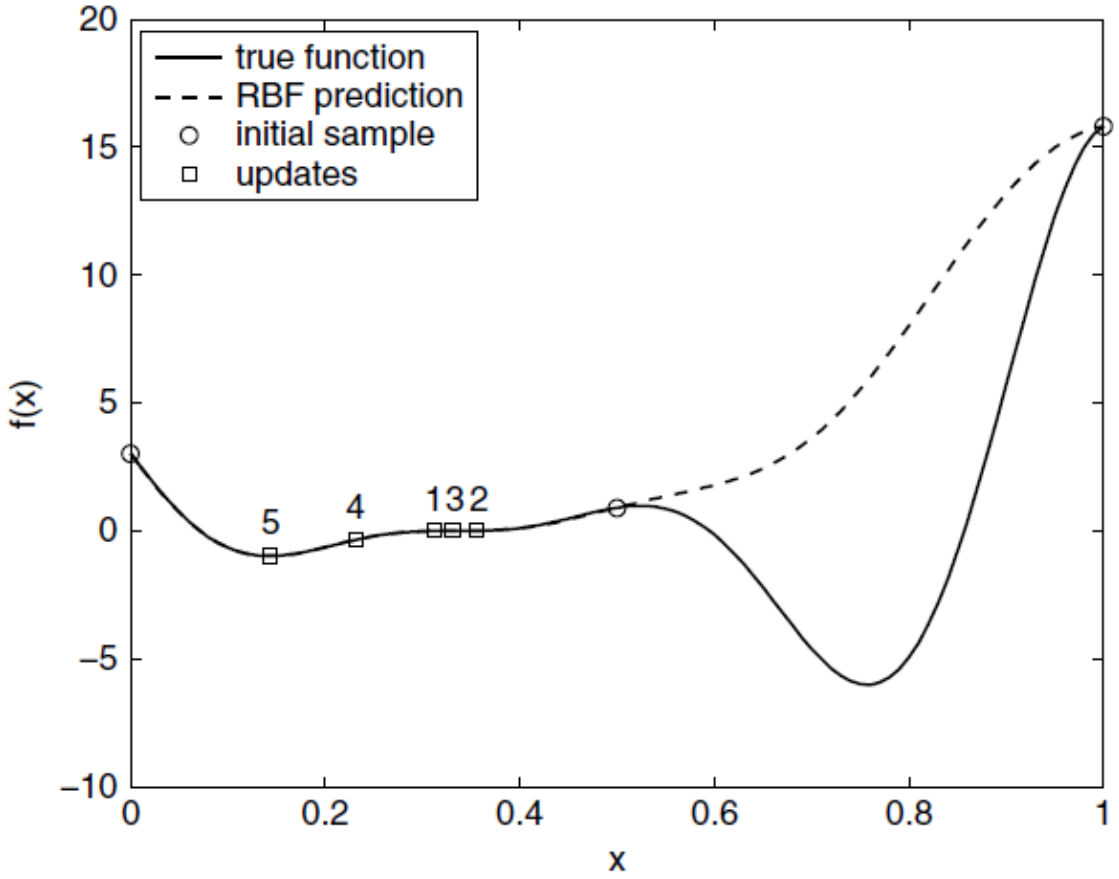

Figure 3: A minimum prediction based infill strategy for Gaussian RBF prediction [35]

Equation (2.31) is interpreted graphically in Figure 4 which shows the prediction in Figure 3 along with a vertical Gaussian distribution with variance $s^2(\boldsymbol{x})$ centered around the prediction $\hat{y}(\boldsymbol{x})$. The Gaussian distribution represents the uncertainty in the prediction and the area enclosed by the distribution below the best observed value so far, y_{min}, is the Probability of Improvement. The Expected Improvement is the first moment of area enclosed by the Gaussian distribution below the best observed value.

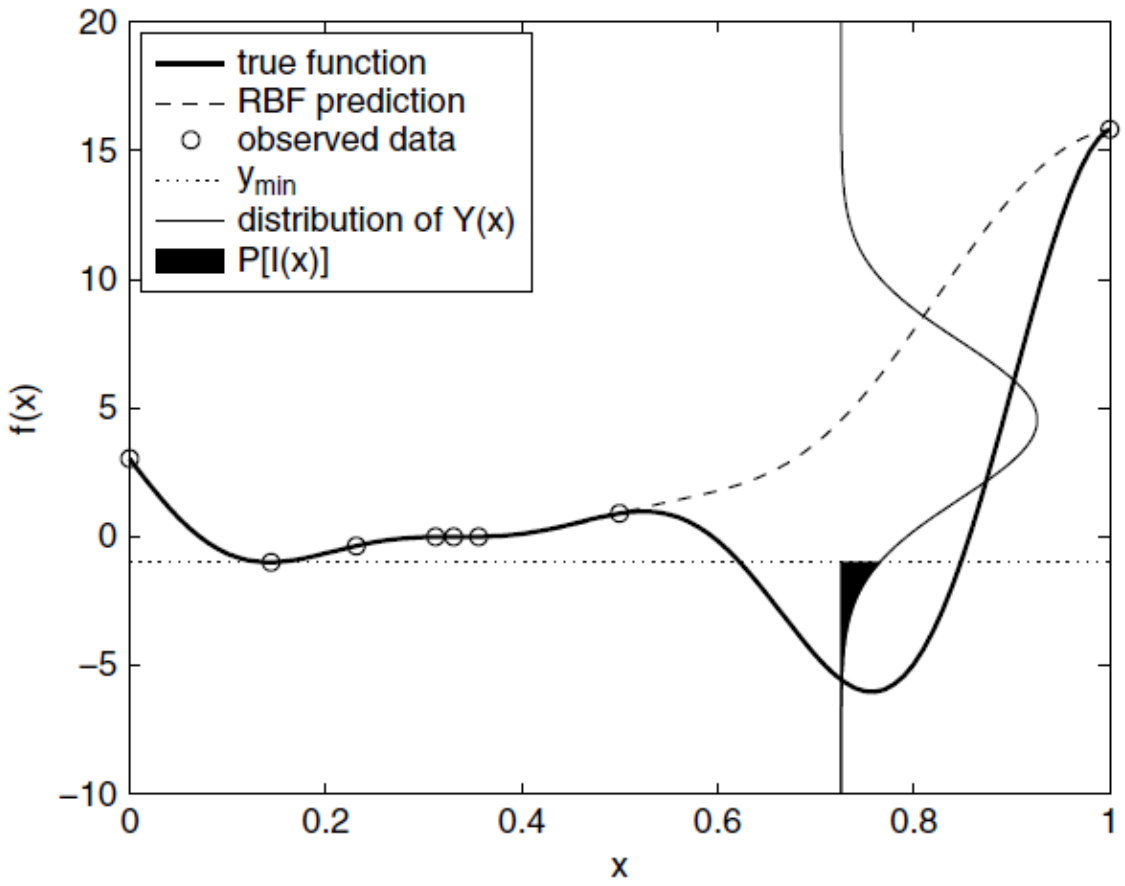

Figure 4: A graphical interpretation of the probability of improvement [35]

In the current work, the Efficient Global Optimization (EGO) algorithm [41] was used to find the best design possible. The Probability of Improvement and Expected Improvement were used as acquisition functions. After finding the initial best design, i.e., the maximum value of neck size from the simulation response values, the acquisition function is maximized using a genetic algorithm [42]. The optimal values of the design variables are determined and using those values, the new response is found out from the simulation model. This helps in updating the metamodel in each iteration. This process is continued till an adequately suitable design is obtained or until the maximum number of iterations i.e., 15 is reached. The following flowchart illustrates the workflow of the optimization routine.

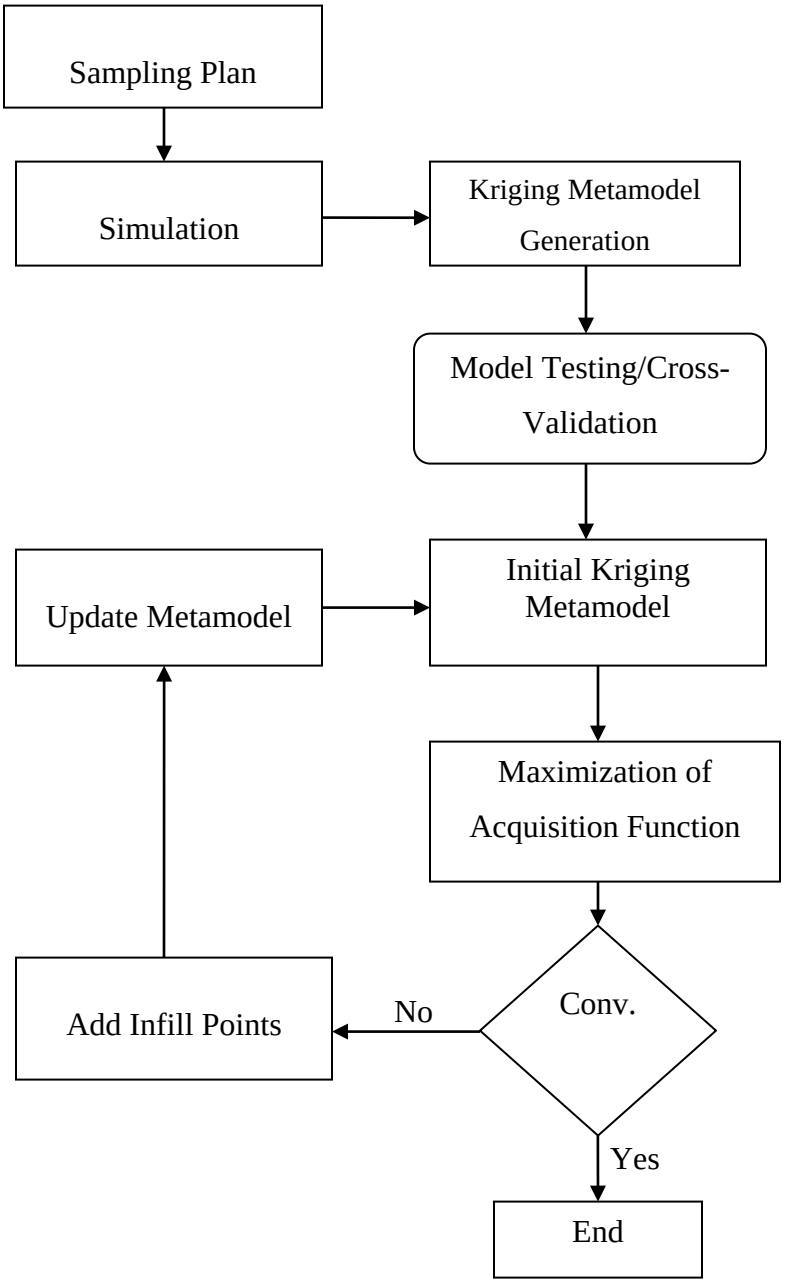

Figure 5: Efficient Global Optimization (EGO) algorithm

The optimization problem for equal-sized particles can be framed as

$$\begin{aligned} &\text{find} && \boldsymbol{x} \in \mathbb{R}^2 \\ &\text{maximize} && N(x) \\ &\text{subject to} && x_i \in \{4{,}40, \ldots, 24{,}41.5\} \end{aligned}$$

where $\boldsymbol{x} = \left(D_{surf}, d\right)$ is the vector of design variables surface diffusivity and inter-particle distance, and $N(\boldsymbol{x})$ is the neck size.

The Efficient Global Optimization (EGO) approach was used in this work for the following major advantages [41]:

- Fewest function evaluations are required among other competing optimization methods. This is due to the possibility of interpolating or extrapolating accurately over large distances in the design space.
- There is a credible stopping rule based on the acquisition function from further searching the surrogate. This is possible because the probabilistic model provides confidence intervals on the function's value at unsampled points, the validity of which can be checked by model validation techniques.
- There is a fast approximation to the multi-physics simulation model that can be used to identify important variables and visualize the nature of input-output relationships.

3. RESULTS AND DISCUSSION

3.1 Sintered Particle Microstructures from Phase-field Modeling

Figures 6-9 depict the microstructure evolution with the sizes of the two spherical particles being equal, using the phase-field code in Ref. [33]. In this case, it can be observed that the shrinkage of both particles takes place at an equal rate. The neck evolution is rapid at the beginning and then slows down later. The changes in the size of the neck can be attributed to the transport of matter from regions in the vicinity with high concentration to the neck region facilitated by various diffusion paths. The neck sizes at time steps 100, 5000, 12,500 and 20,000 are 9.02257, 17.36433, 20.96770 and 22.47932 respectively.

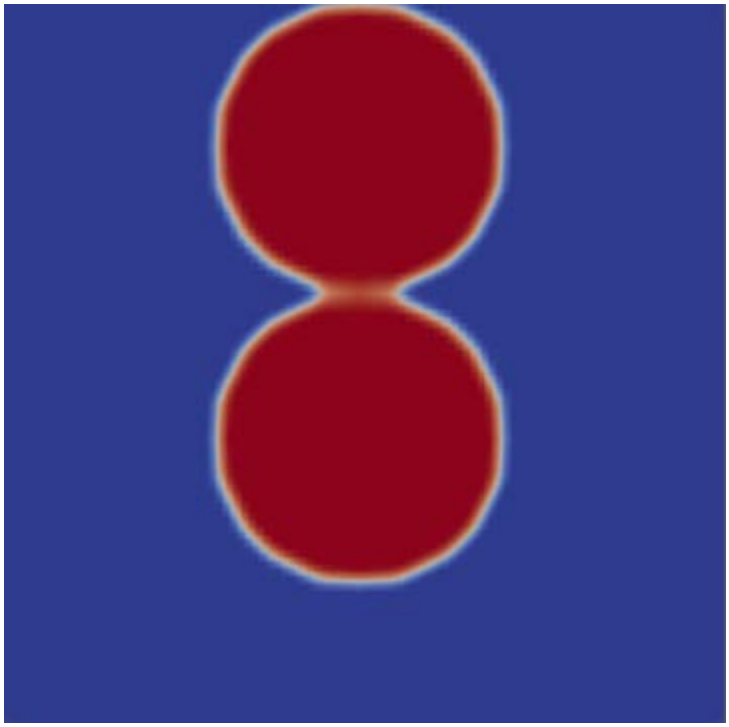

Figure 6: Neck evolution at time step 100 for equal-sized particles

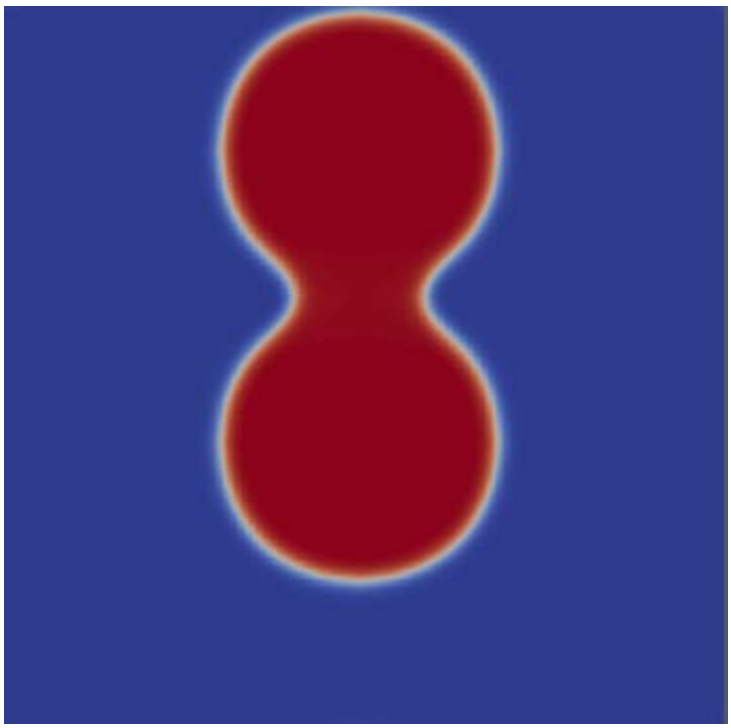

Figure 7: Neck evolution at time step 5000 for equal-sized particles

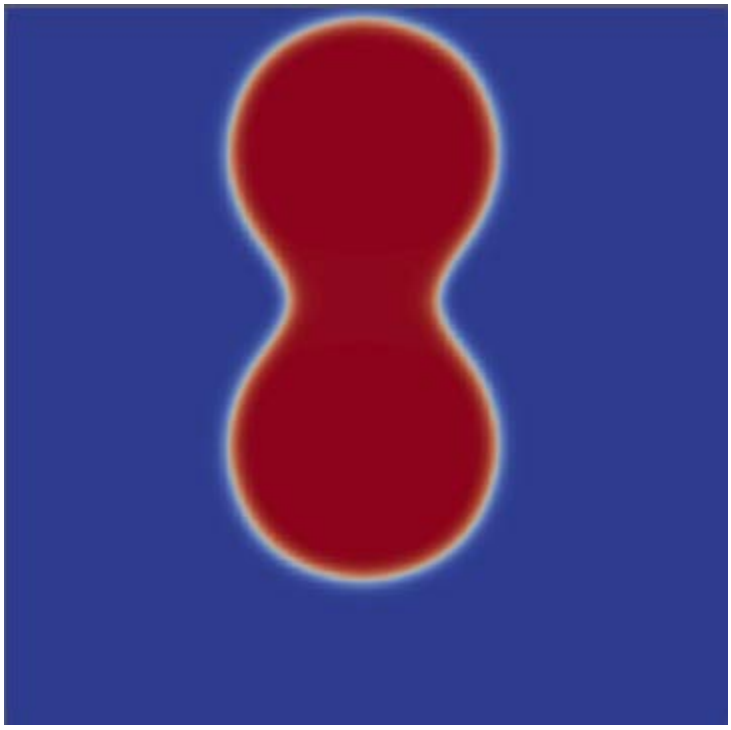

Figure 8: Neck evolution at time step 12,500 for equal-sized particles

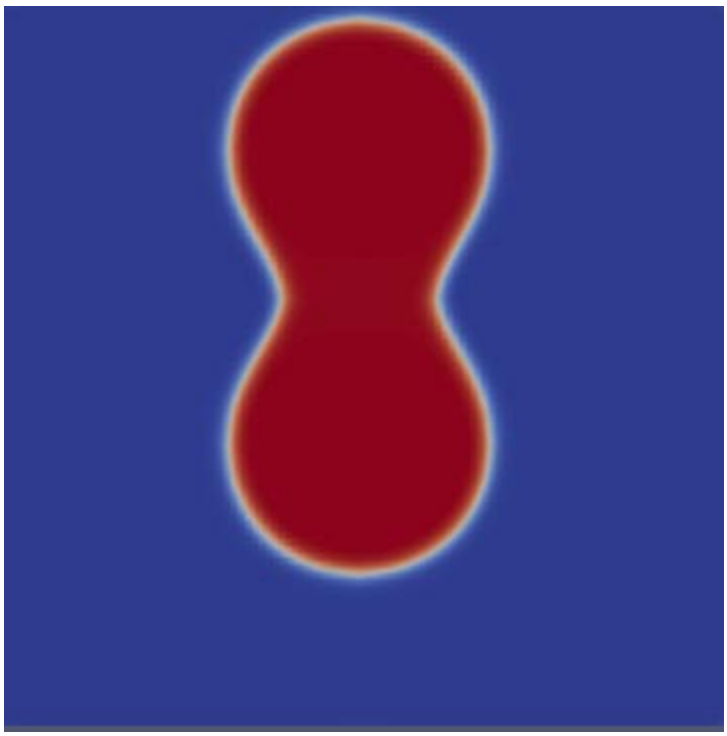

Figure 9: Neck evolution at time step 20,000 for equal-sized particles

Figures 10-13 describe the evolution of the neck region for unequal sized particles, i.e., particle size ratio of 1.5, using the phase-field code in Ref. [33]. It was observed that the neck formation was rapid in the early stages of the simulation but later slowed down and reached a steady state. It was also observed that the smaller particle had a faster contraction. The neck sizes at time steps 100, 5000, 12,500 and 20,000 are 8.18180, 14.80311, 16.82539 and 18.66670 respectively.

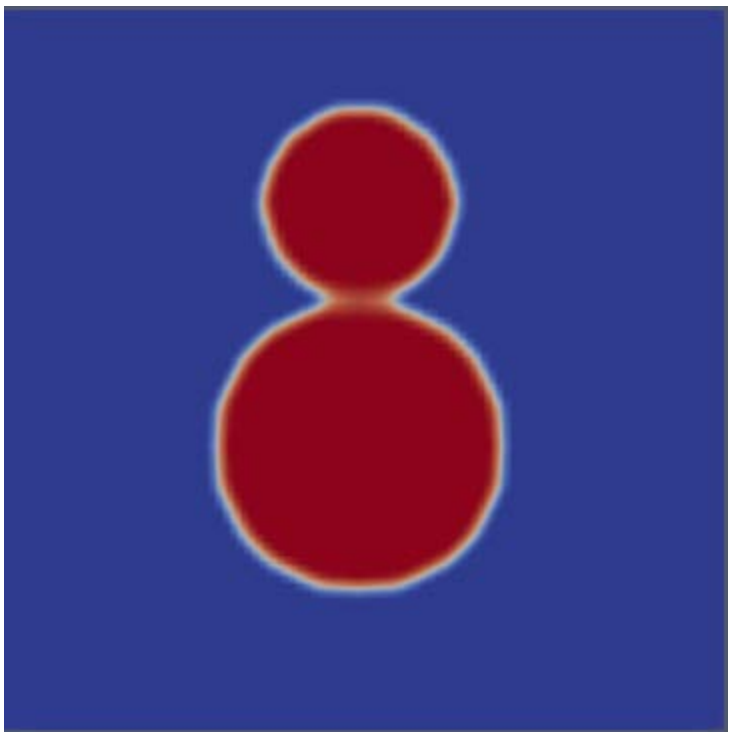

Figure 10: Neck evolution at time step 100 for unequal sized particles

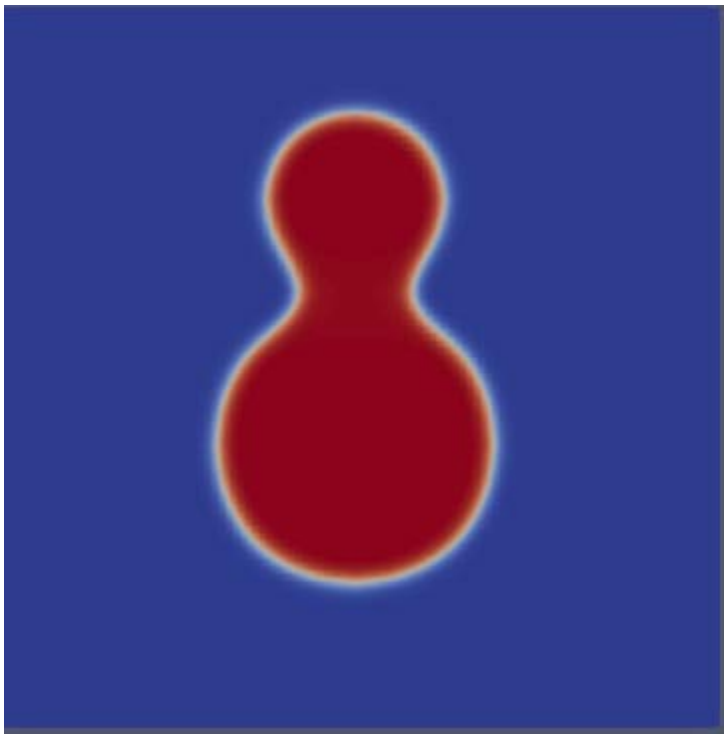

Figure 11: Neck evolution at time step 5000 for unequal sized particles

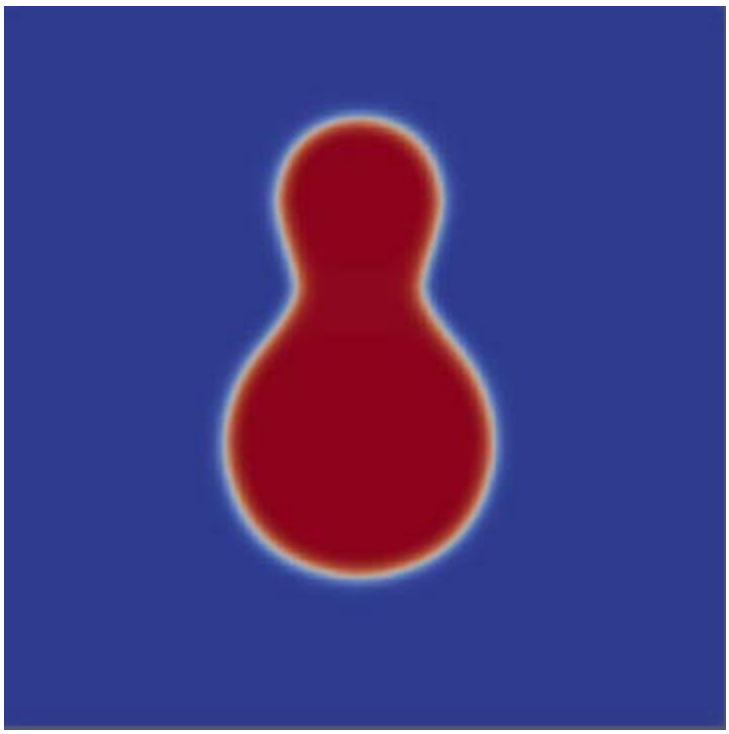

Figure 12: Neck evolution at time step 12,500 for unequal sized particles

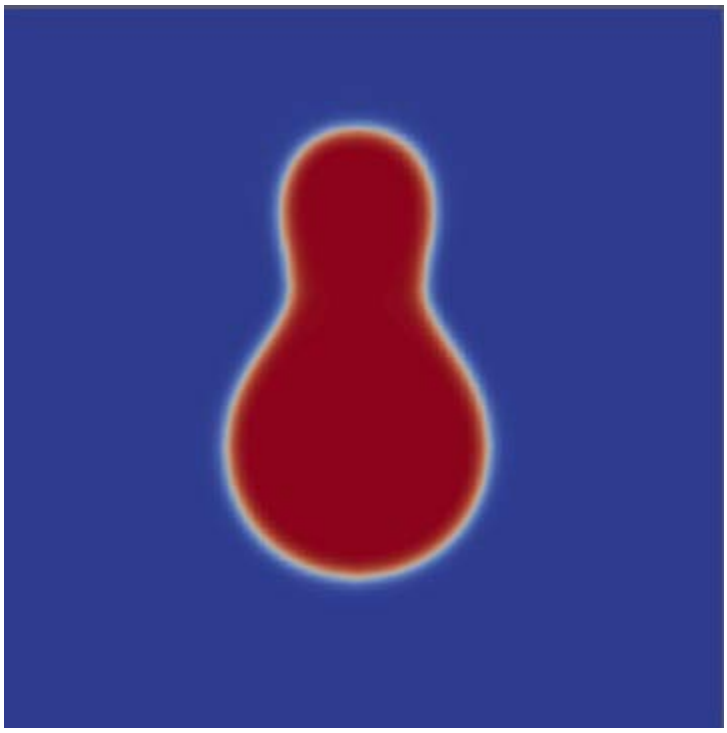

Figure 13: Neck evolution at time step 20,000 for unequal sized particles

Figure 14 below shows the nature of evolution of the neck region for both equal and unequal sized particles. The curve showing increase of neck size is steep at the beginning for both the particle sizes and then tends to flatten as the time step increases. In both cases, the surface diffusivity was fixed at 16. This indicates that the particle size does not have a significant effect on the evolution of neck size at later time steps.

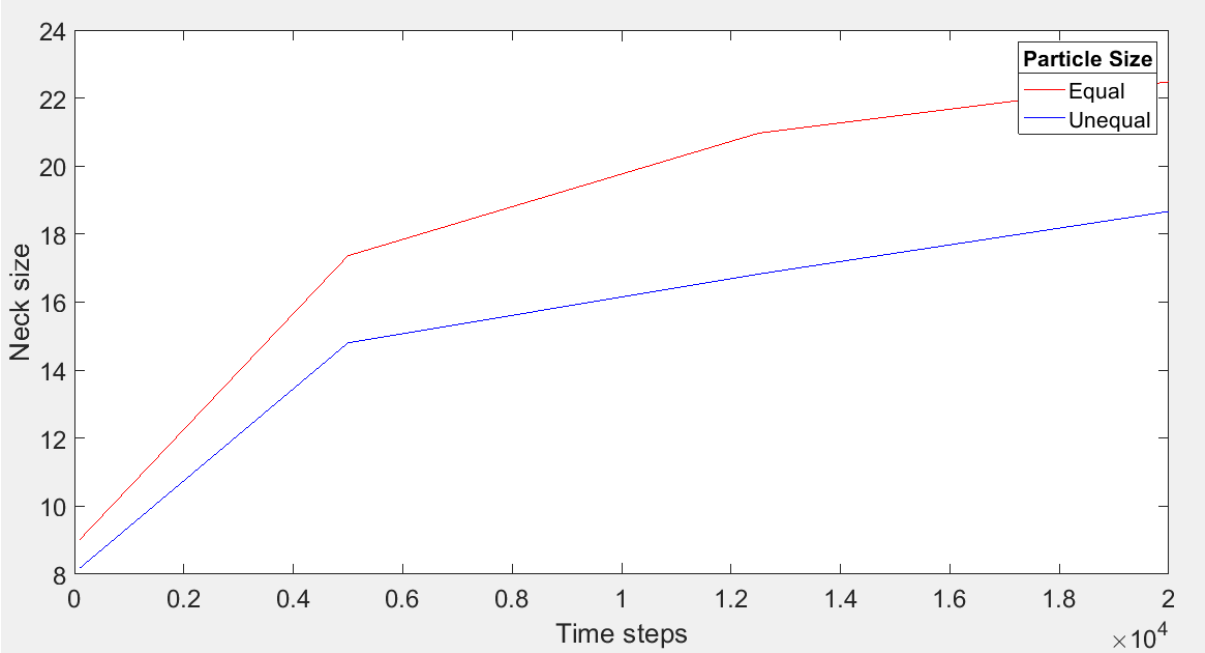

Figure 14: Evolution of neck size at different time steps for equal and unequal sized particles

3.2 Machine Learning Results

3.2.1 Equal Sized Particles

A. Initial Metamodel Generation

Figures 15-17 show the initial metamodels obtained using three regression functions of order zero (Regpoly0), one (Regpoly1) and two (Regpoly2) respectively. The neck size is seen to increase with increasing surface diffusivity and decreases with increasing inter-particle distance.

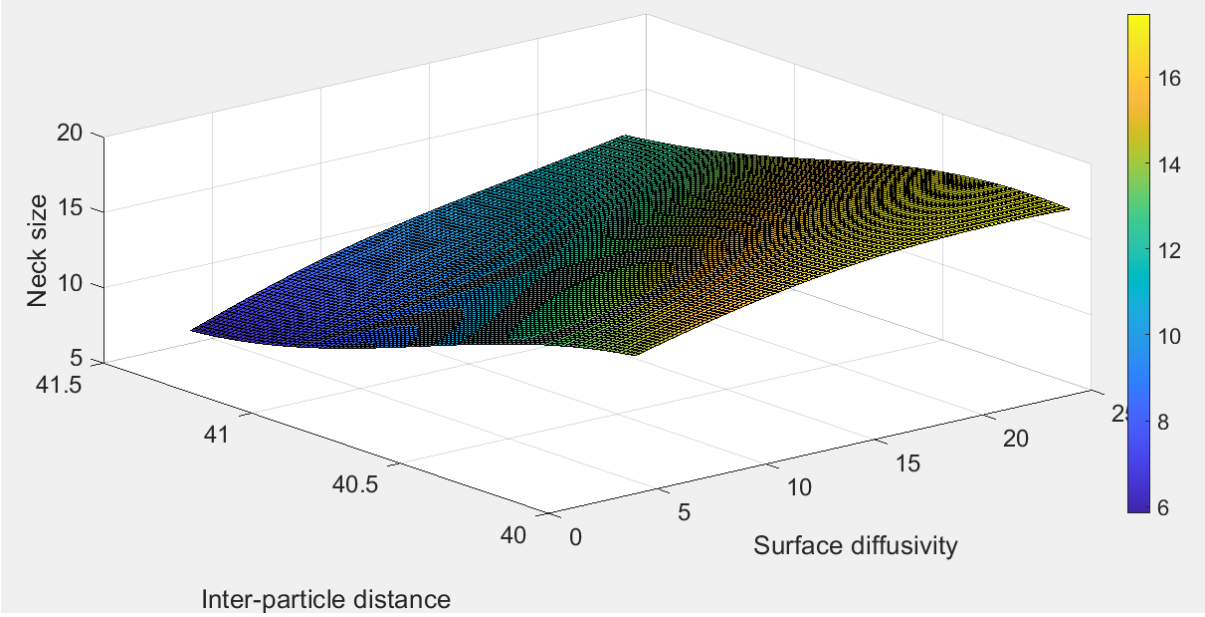

Figure 15: Metamodel by Regression Function of Order Zero

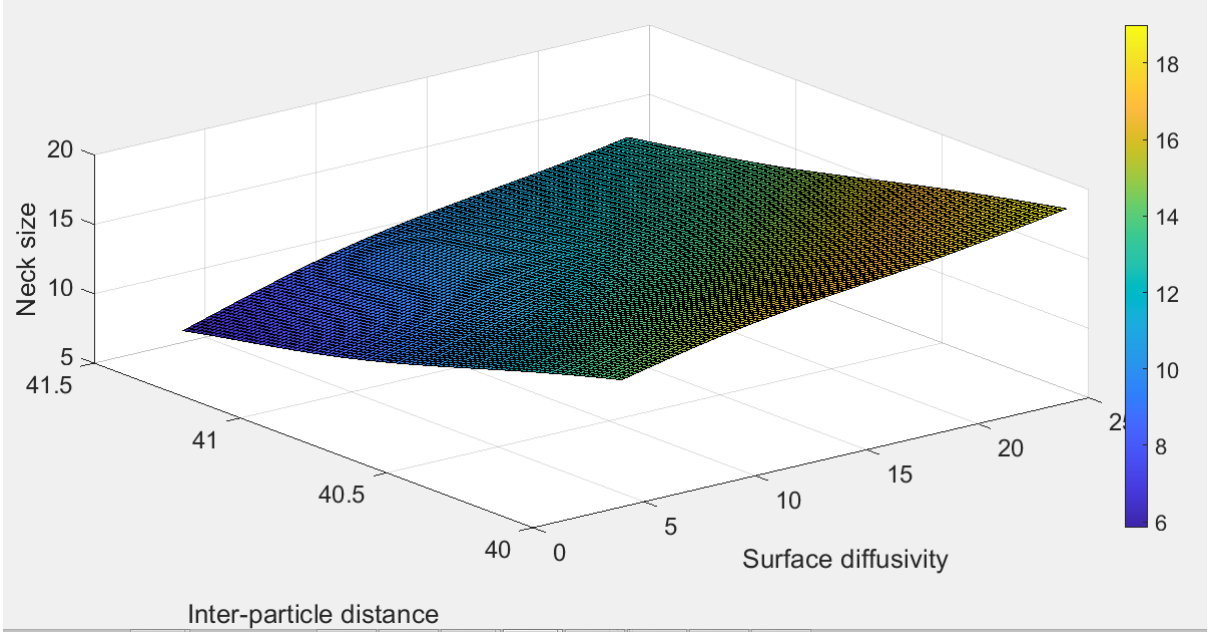

Figure 16: Metamodel by Regression Function of Order One

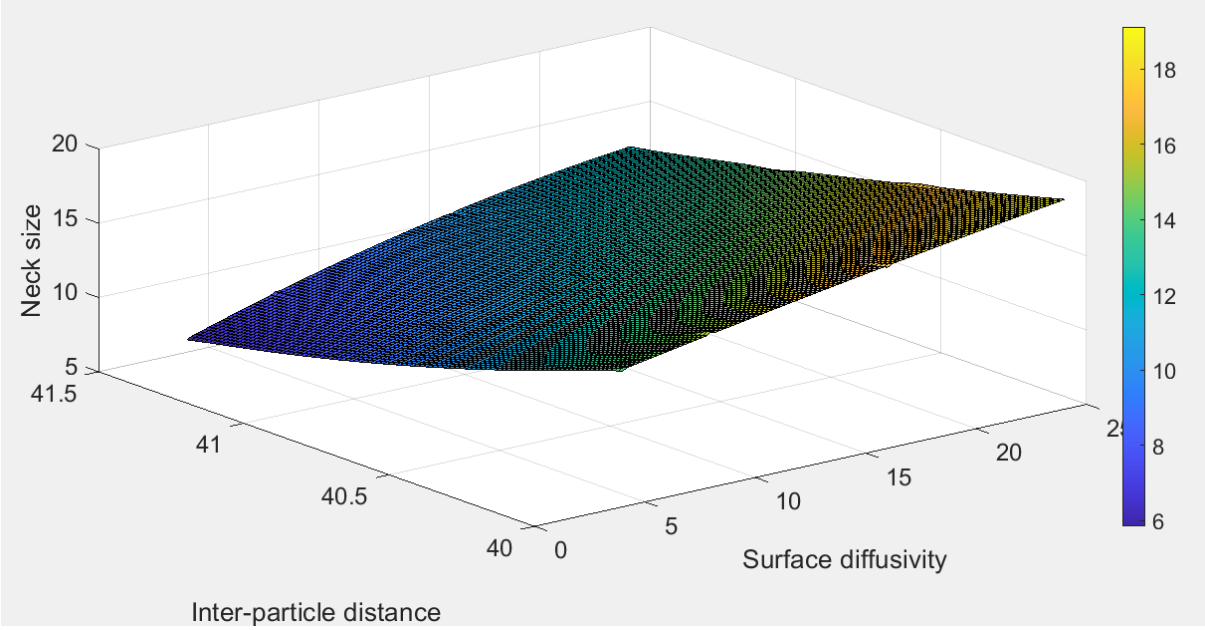

Figure 17: Metamodel by Regression Function of Order Two

B. Model Testing

Table 7 below shows the root mean square error (RMSE) values for each initial metamodel. The model with regression function of order zero was found to have the least RMSE of 1.2077 and hence was selected for further optimization process.

Table 7: RMSE values at different regression functions for equal-sized particles

Particle size	Regpoly0	Regpoly1	Regpoly2
Equal	1.2077	1.2205	1.3937

C. Cross-Validation

Table 8 shows the average error found by cross-validation for the observations used to build the surrogate model of equal-sized particles. The model with regression function of order zero has the least error of 0.25836. Hence error results from both model testing and cross-validation indicate Regpoly0 is the best metamodel for equal-sized particles.

Table 8: Cross-Validation errors for equal-sized particles

Particle size ratio	Regpoly0	Regpoly1	Regpoly2
Equal	0.25836	0.38635	0.32083

D. Sensitivity Analysis

Figures 18 and 19 show the correlation of surface diffusivity and inter-particle distance with neck size respectively. Figure 18 points out a strong correlation with correlation coefficient of 0.5733 explaining that as the surface diffusivity increases, there is a large increase in neck size. Figure 19 explains that the inter-particle distance is strongly associated with the neck size with a Pearson correlation coefficient of -0.8028. As the inter-particle distance increases, there is a large decrease in neck size.

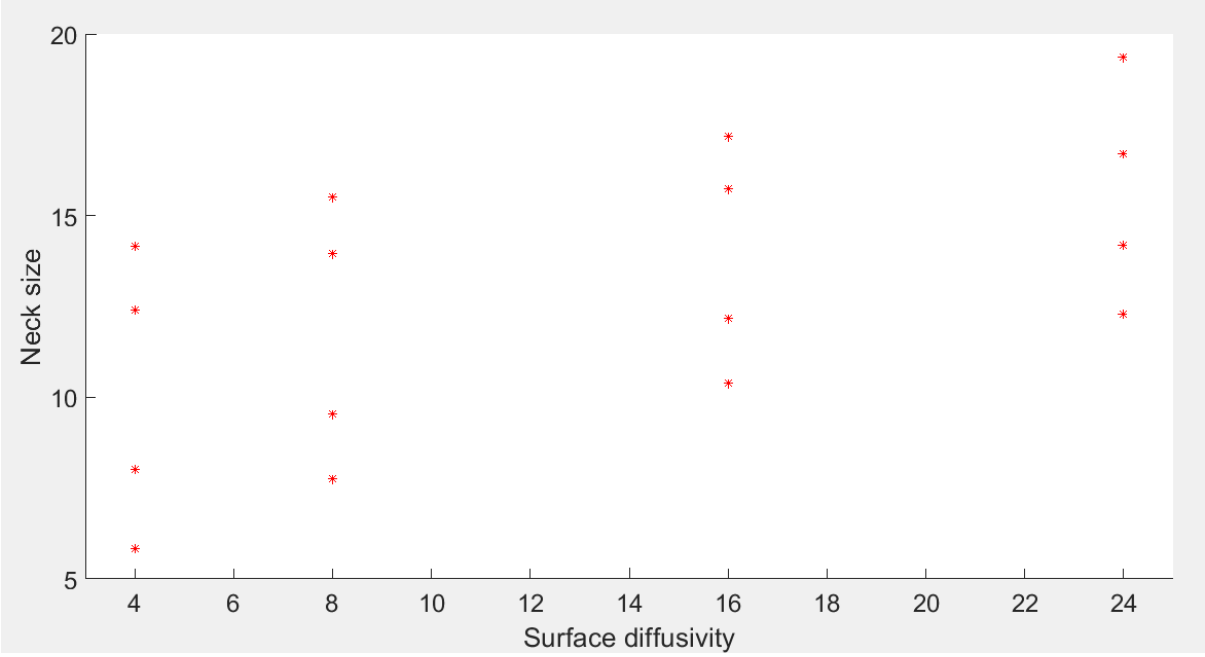

Figure 18: Correlation between surface diffusivity and neck size for equal-sized particles

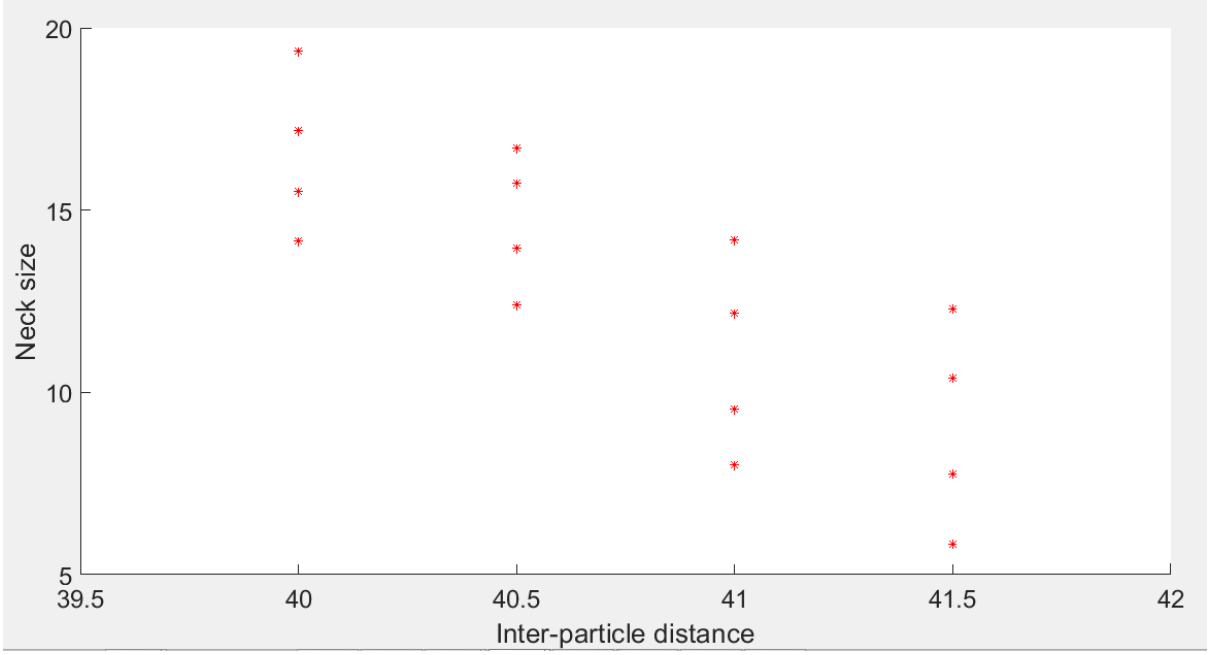

Figure 19: Correlation between inter-particle distance and neck size for equal-sized particles

E. Optimization by Probability of Improvement

Figures 20 and 21 show the first iteration of input parameter optimization using Probability of Improvement (PI) as the acquisition function. Figure 20 illustrates the random sampling plan with surface diffusivity ranging from 4 to 24 and inter-particle distance from 40 to 41.5. Figure 21 shows the first metamodel generated by Gaussian Process Regression and explains the monotonic nature of the data for neck size linearly increasing with increasing surface diffusivity and decreasing with inter-particle distance.

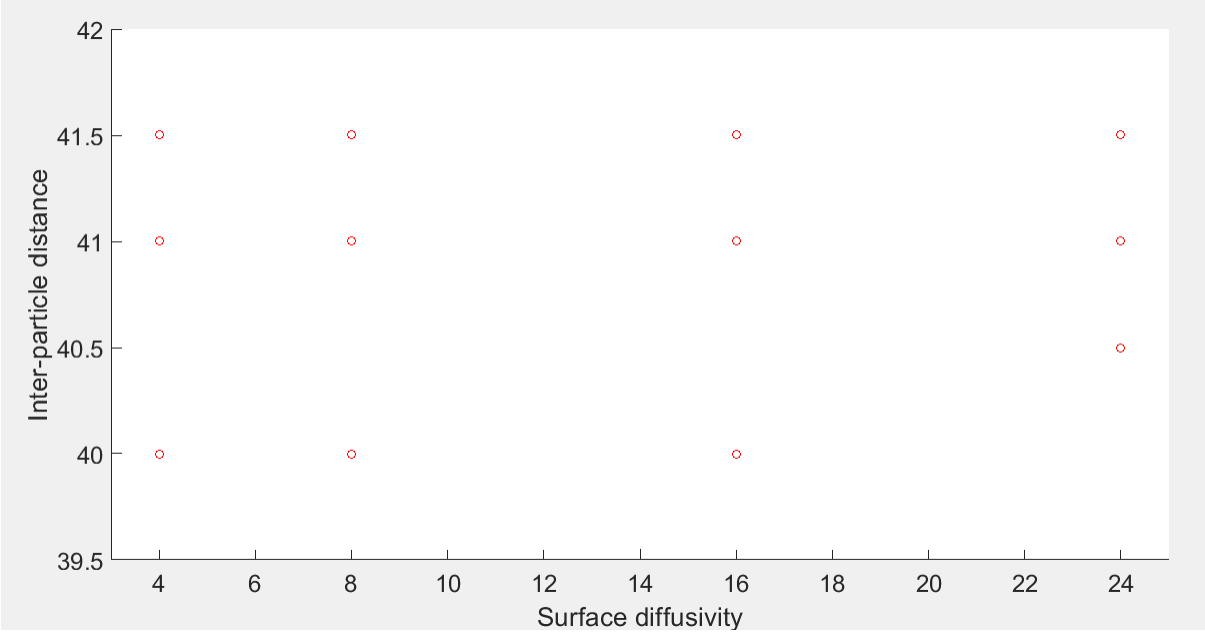

Figure 20: Sampling plan for iteration 1 of PI optimization for equal-sized particles

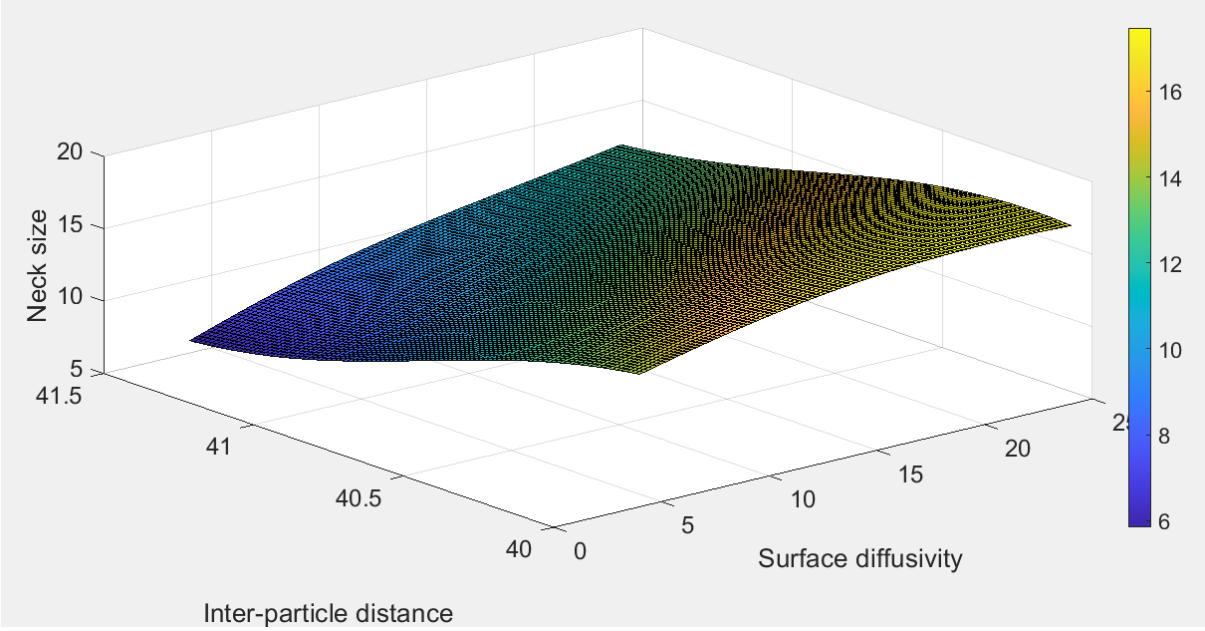

Figure 21: Kriging metamodel for iteration 1 of PI optimization for equal-sized particles

Figures 22 and 23 describe the last iteration in the optimization process. The values of optimal design variables converged after 10 iterations at [23.8268, 40.0001]. Hence the iteration was stopped here. The maximum neck size was 19.0476 and the Probability of Improvement 0.5119.

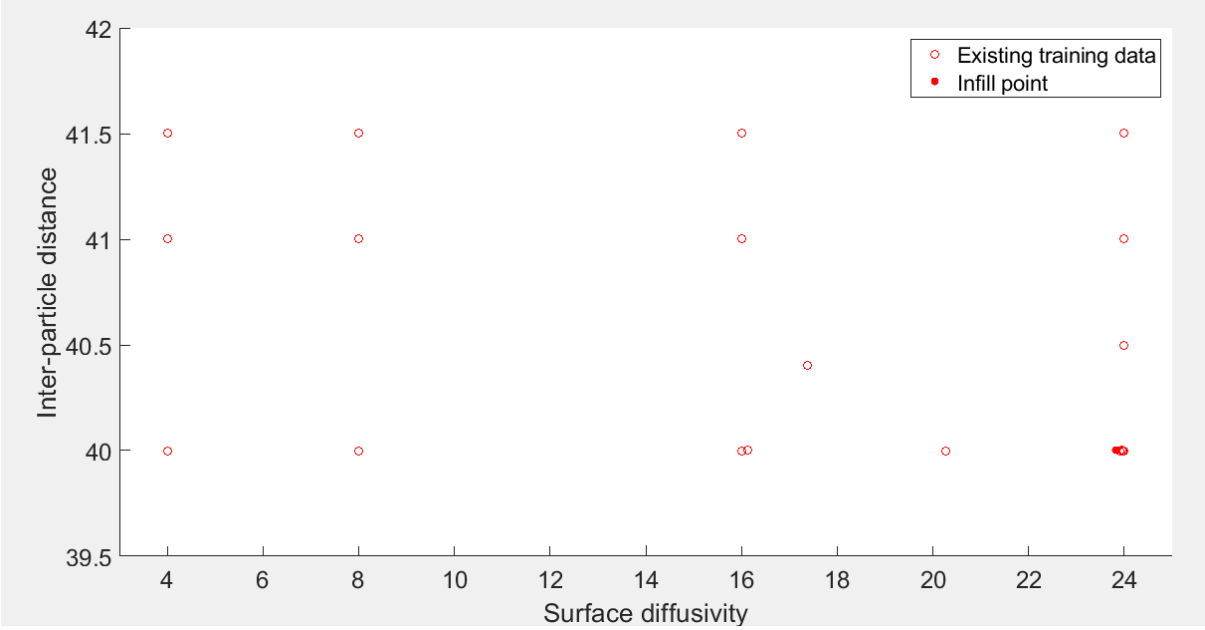

Figure 22: Sampling plan for iteration 10 of PI optimization for equal-sized particles

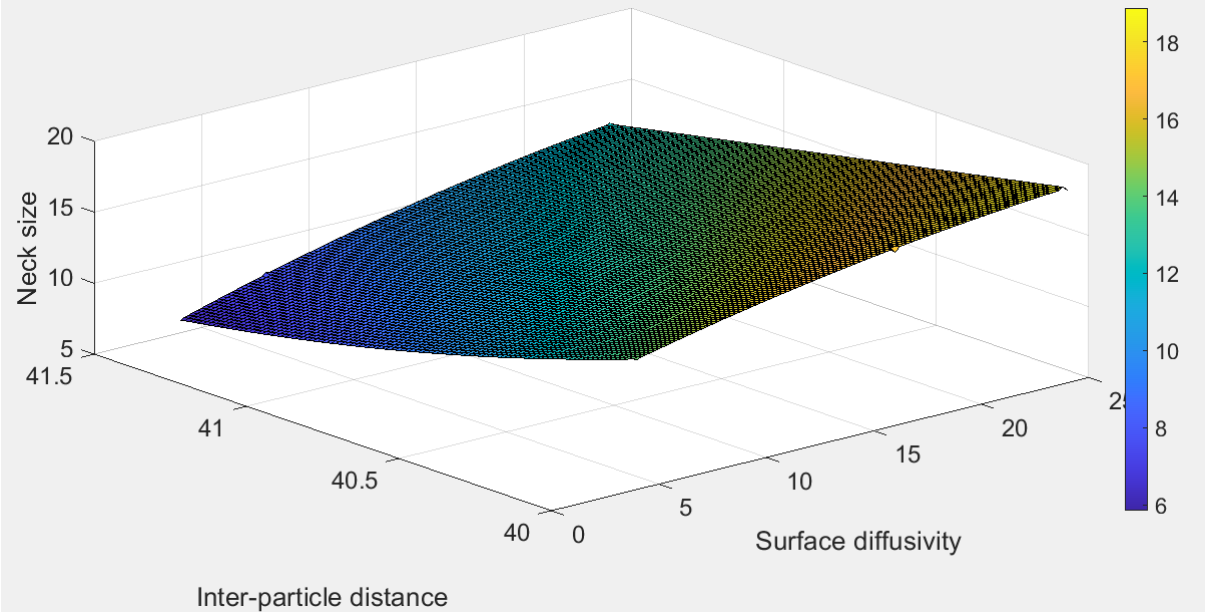

Figure 23: Kriging metamodel after iteration 10 of PI optimization for equal-sized particles

F. Optimization by Expected Improvement

Figures 24 and 25 show the first iteration of design optimization using Expected Improvement (EI) as the acquisition function. Figure 24 displays the random sampling plan with surface diffusivity ranging from 4 to 24 and inter-particle distance from 40 to 41.5. Figure 25 shows the

initial metamodel generated by Kriging regression and re-iterates the fact that the neck size linearly increases with increasing surface diffusivity and decreases with increasing inter-particle distance.

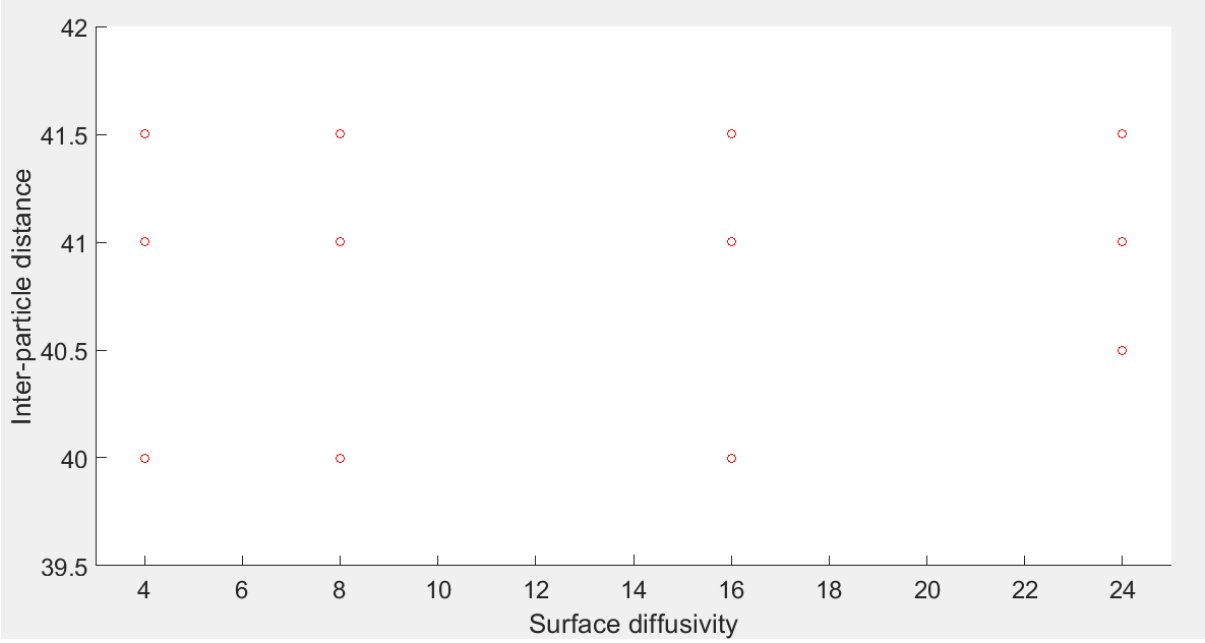

Figure 24: Sampling plan for iteration 1 of EI optimization for equal-sized particles

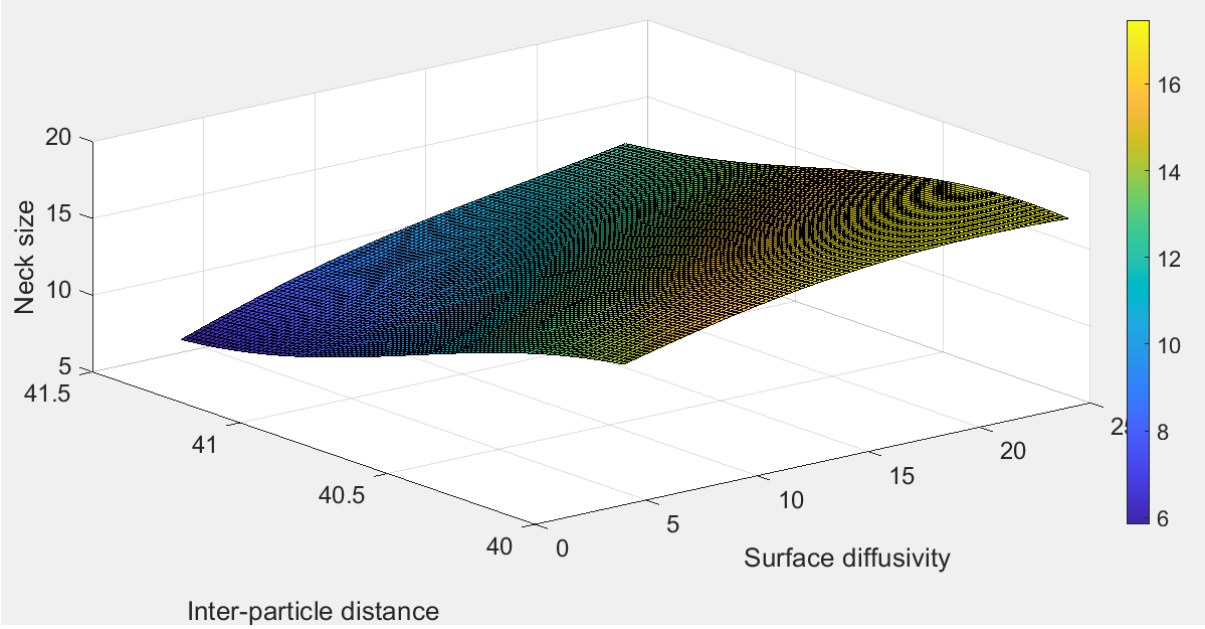

Figure 25: Kriging metamodel for iteration 1 of EI optimization for equal-sized particles

Figures 26 and 27 demonstrate the last iteration in the optimization process. After 15 iterations were used up, the values of optimal design variables were found as [23.9874, 40.7428]. The maximum neck size was 19.0476 and the Expected Improvement 8.1805E+03. The solution obtained looks like a global optimum as all potential values seem to have been explored from the entire design space.

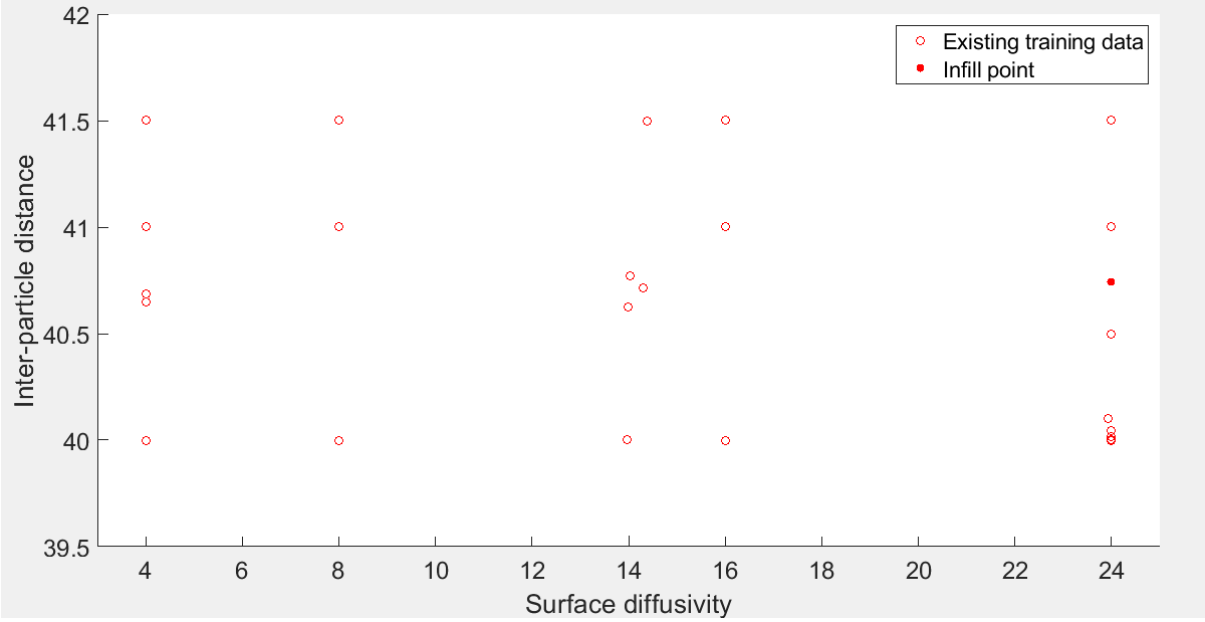

Figure 26: Sampling plan for iteration 15 of EI optimization for equal-sized particles

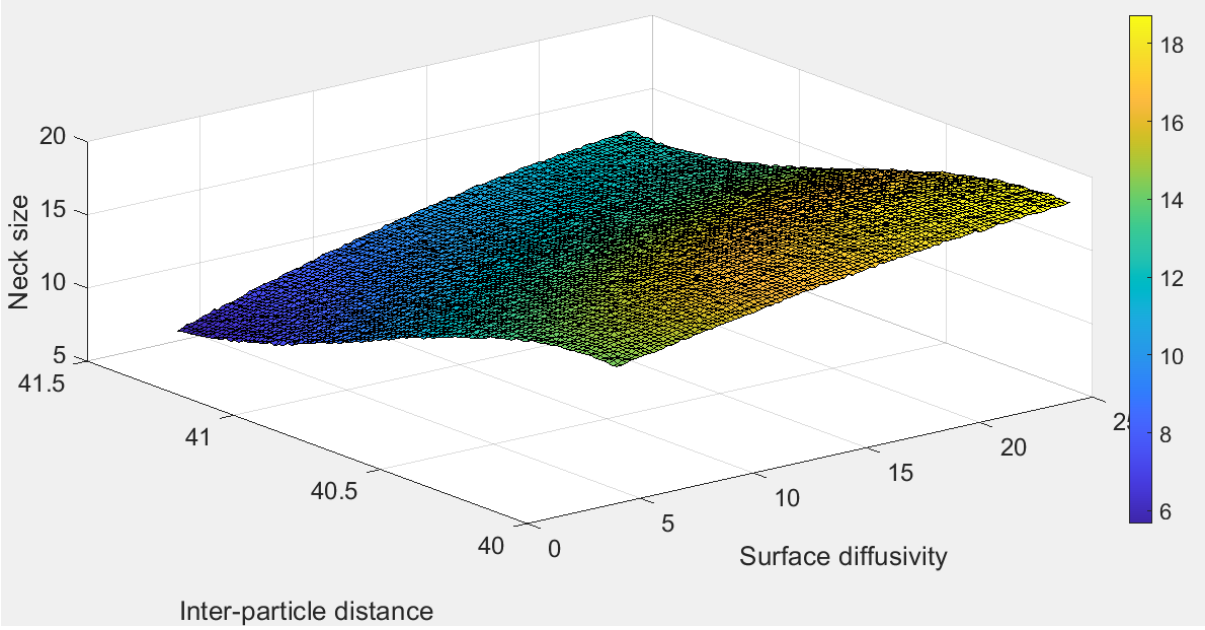

Figure 27: Kriging metamodel for iteration 15 of EI optimization for equal-sized particles

Figure 28 shows how the Probability of Improvement is varying with each iteration for equal-sized particles. It gradually decreases as the iterations proceed. The design converges after 10 iterations.

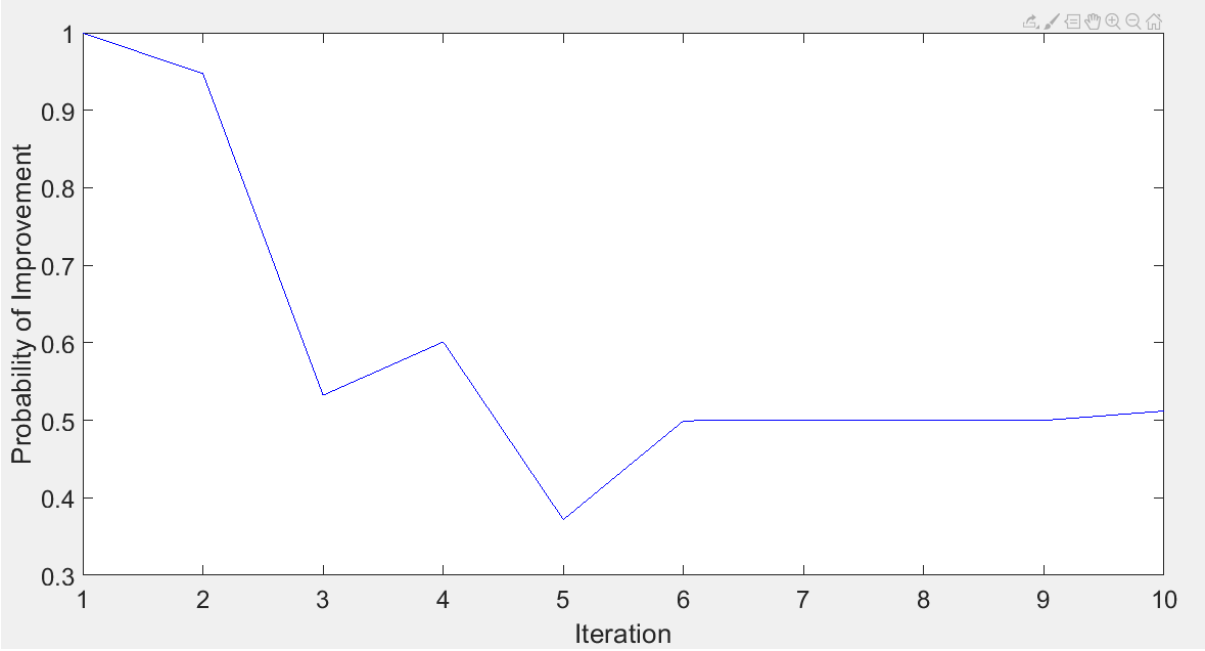

Figure 28: Probability of Improvement at each iteration for equal-sized particles

Figure 29 presents the Expected Improvement at each iteration for equal-sized particles. The EI tends to decrease after each iteration but seems to require more number of iterations to finally become zero. This might be because the function is trying to explore the entire design space for possible infill points.

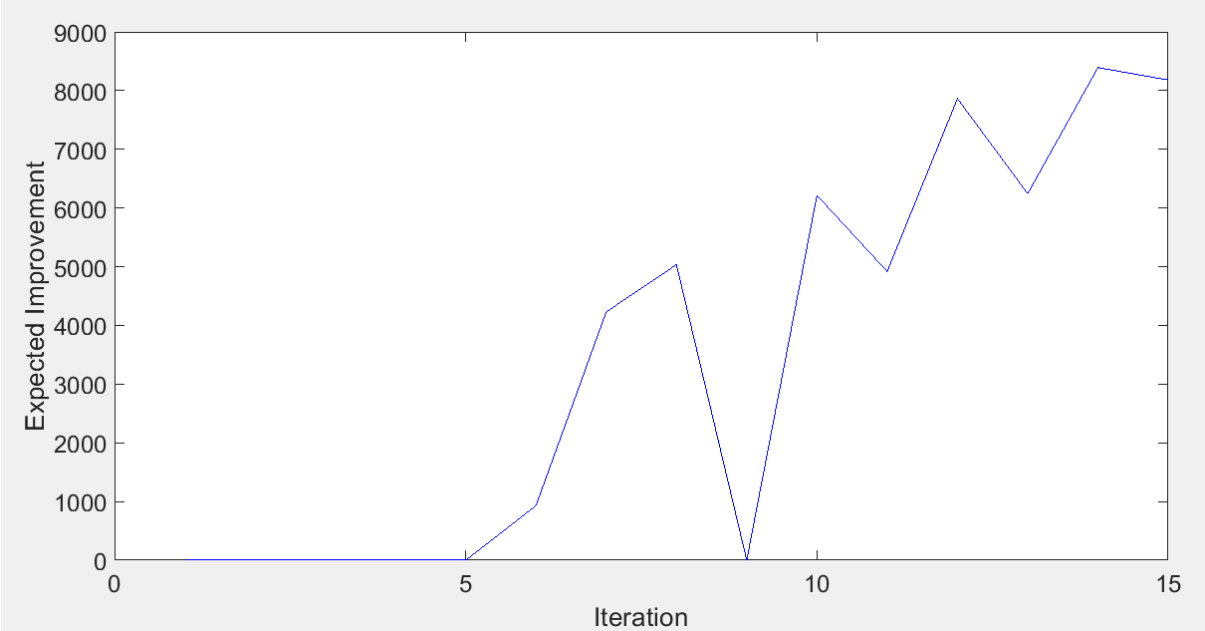

Figure 29: Expected Improvement at each iteration for equal-sized particles

Figures 30 and 31 detail the responses sampled by PI and EI at each iteration to update the Kriging surrogate. Some samples are used to exploit the surrogate while others are used to explore the design space. The optimal solutions were found after 10 and 15 iterations respectively.

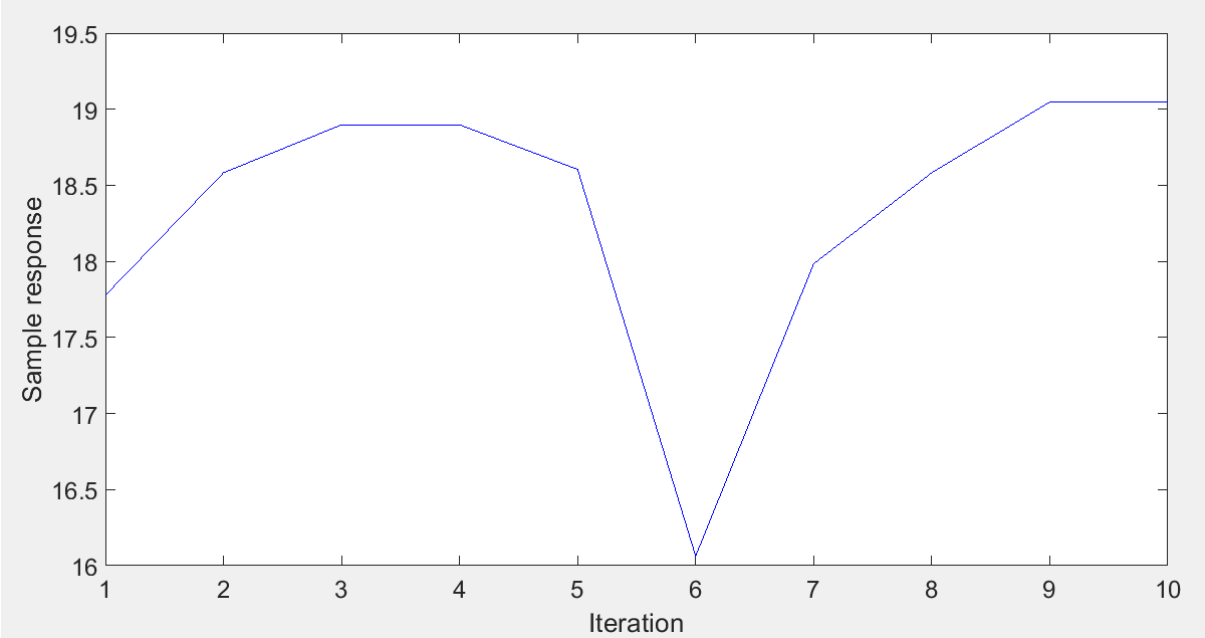

Figure 30: Response of the designs sampled by PI for equal-sized particles

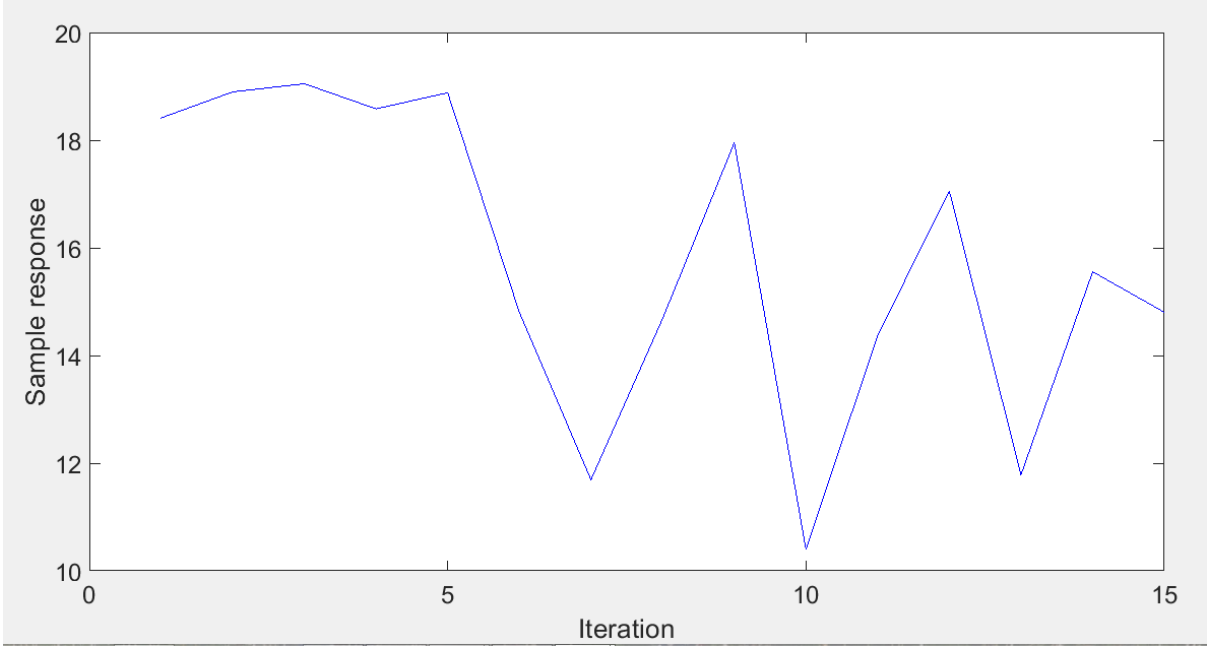

Figure 31: Response of the designs sampled by EI for equal-sized particles

3.2.2 Unequal Sized Particles

A. Initial Metamodel Generation

Figures 32-34 show the initial metamodels obtained using three regression functions of order zero (Regpoly0), one (Regpoly1) and two (Regpoly2) respectively. The figures have surfaces that detail the monotonic increase of neck size with increase in surface diffusivity and decreasing neck size with increase in inter-particle distance. The neck size increased from 12.093 to 14.68752 for inter-particle distance of 33.3, from 6.82169 to 12.06348 for inter-particle distance of 34.3 and from 4.30771 to 10.39367 for inter-particle distance of 34.8. The surface diffusivity ranged from 4 to 24 and inter-particle distance spanned 33.3 through 34.8.

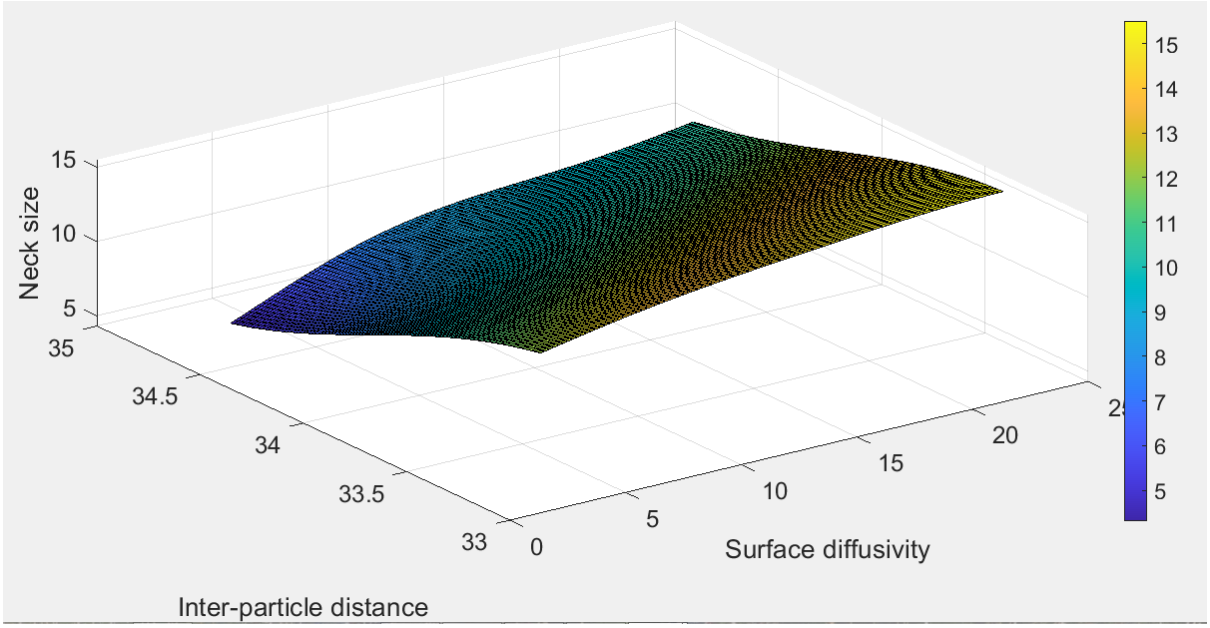

Figure 32: Metamodel by Regression Function of Order Zero for unequal sized particles

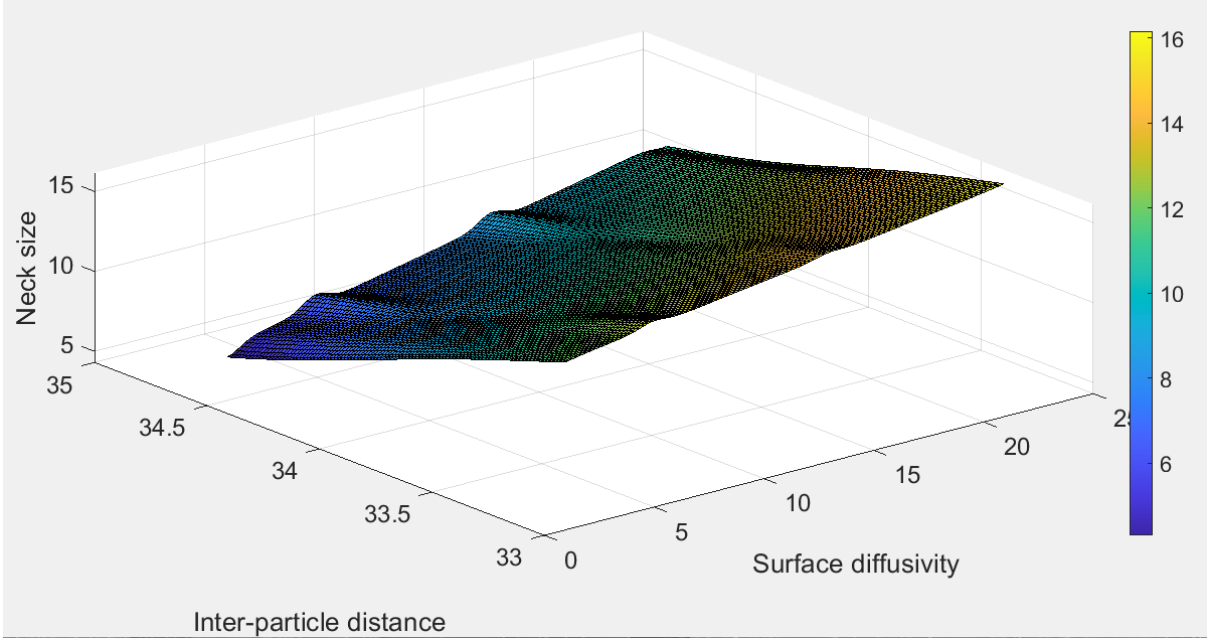

Figure 33: Metamodel by Regression Function of Order One for unequal sized particles

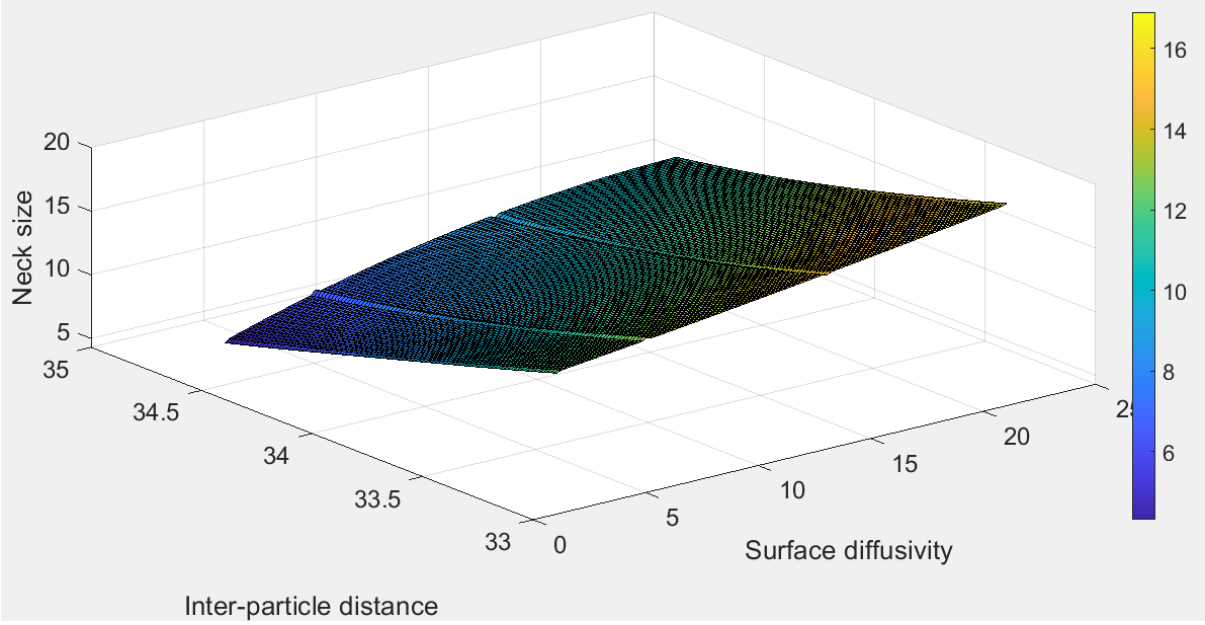

Figure 34: Metamodel by Regression Function of Order Two for unequal sized particles

B. Model Testing

Table 9 below shows the root mean square error (RMSE) values for each metamodel. The model with regression function of order zero was found to have the least RMSE of 0.4111 and hence

was chosen for Bayesian optimization. For both equal and unequal sized particles, the model with regression function of order zero gave the least mean square error. Also, the error was observed to decrease for unequal sized particles.

Table 9: RMSE values at different regression functions for unequal sized particles

Particle size	Regpoly0	Regpoly1	Regpoly2
Unequal	0.4111	0.7734	1.0878

C. Cross-Validation

Table 10 shows the average error found by leave-one-out cross-validation for the observations used to build the surrogate model of unequal sized particles. The model with regression function of order zero has the least error of 0.3149. The error results from model testing and cross-validation for unequal sized particles indicate Regpoly0 is the suitable metamodel to start the optimization process with. This result concurs with that of equal-sized particles. The cross-validation error is greater for unequal sized particles than equal-sized particles.

Table 10: Cross-Validation errors at different regression functions for unequal sized particles

Particle size	Regpoly0	Regpoly1	Regpoly2
Unequal	0.3149	0.5850	0.4362

D. Sensitivity Analysis

Figures 35 and 36 show the correlation of surface diffusivity and inter-particle distance with neck size respectively for unequal sized particles. As for equal-sized particles, Figure 35 demonstrates a strong positive correlation between surface diffusivity and neck size with a coefficient of 0.5734. Figure 36 explains the strong dependence of neck size on inter-particle distance with a Pearson correlation coefficient of -0.7960. As the inter-particle distance increases, there is a considerable decrease in neck size. This proves that the nature of correlation between the QOI and input parameters is independent of the particle size.

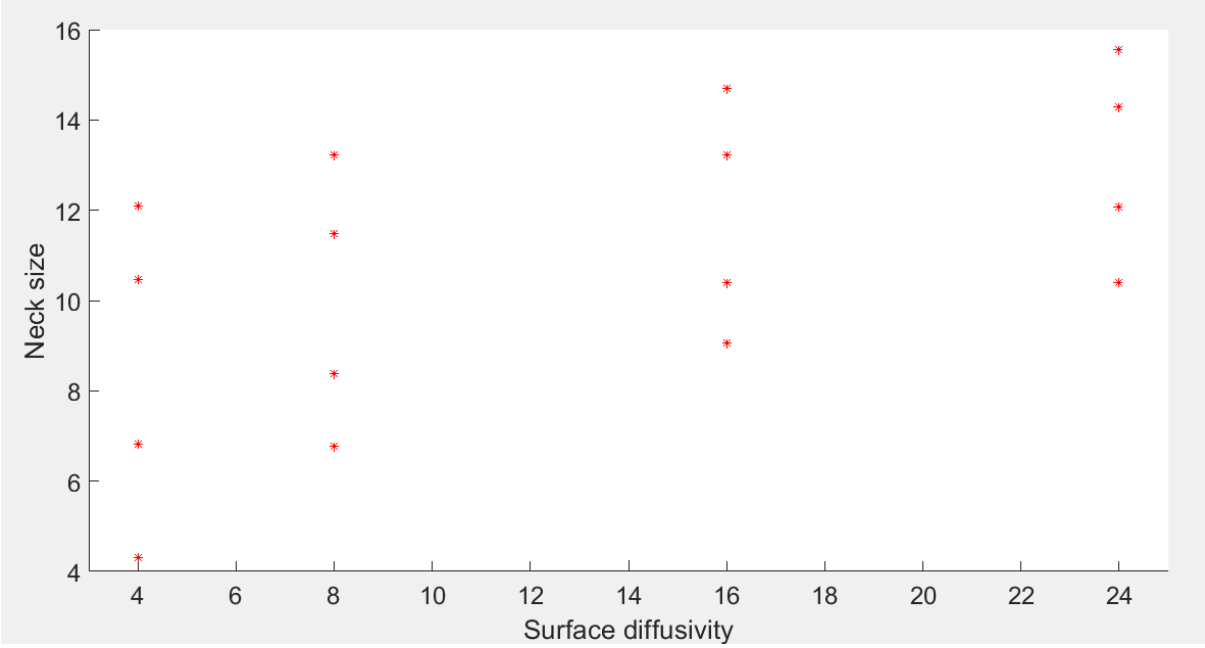

Figure 35: Correlation between surface diffusivity and neck size for unequal sized particles

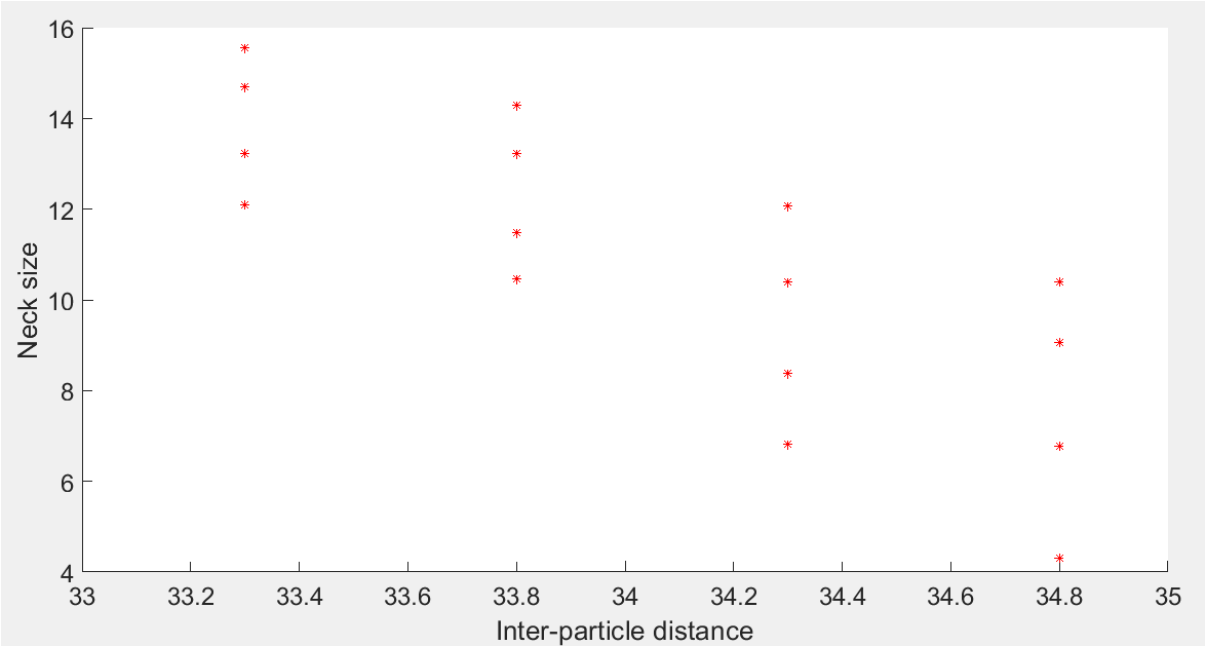

Figure 36: Correlation between inter-particle distance and neck size for unequal sized particles

E. Optimization using Probability of Improvement

Figures 37 and 38 show the first iteration of neck size optimization using Probability of Improvement (PI) as the acquisition function. Figure 37 illustrates the random sampling plan

with surface diffusivity ranging from 4 to 24 and inter-particle distance from 33.3 to 34.8. Figure 38 shows the first metamodel generated by Gaussian Process Regression with neck size linearly increasing for the range of surface diffusivity and decreasing for that of inter-particle distance.

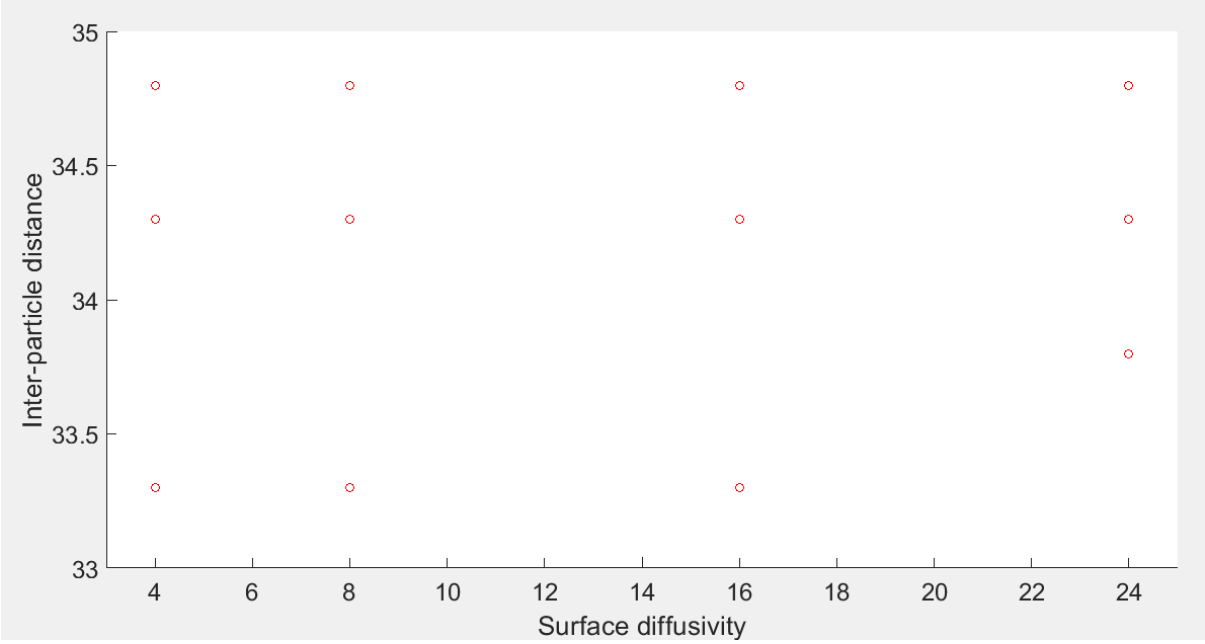

Figure 37: Sampling plan for iteration 1 of PI optimization for unequal-sized particles

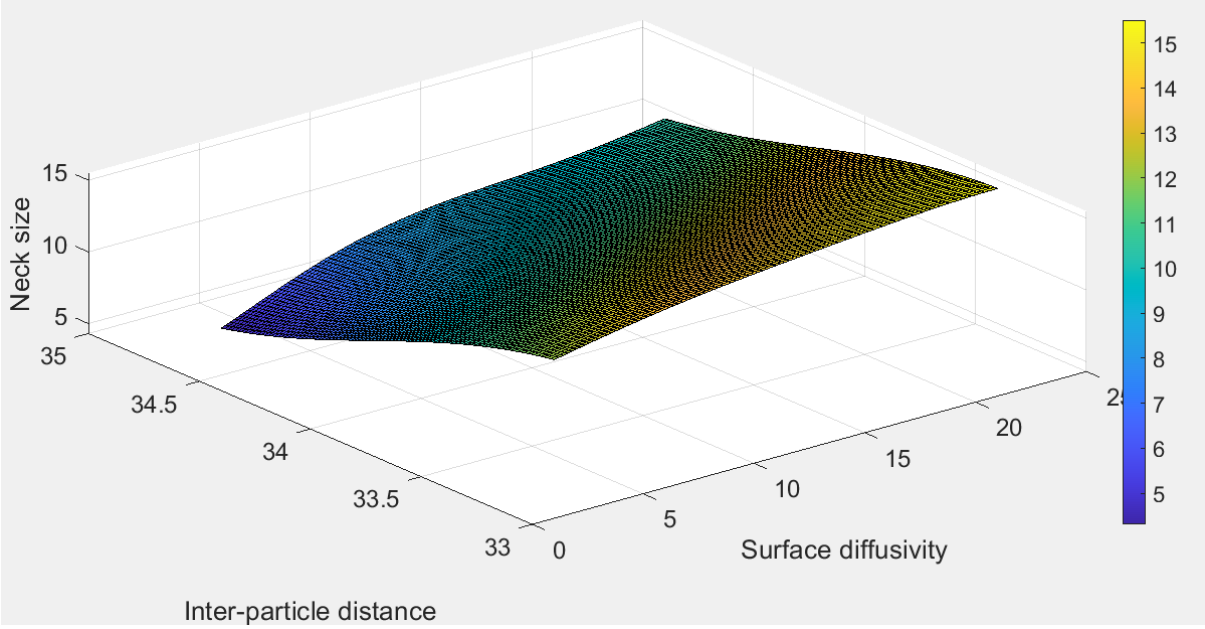

Figure 38: Kriging metamodel for iteration 1 of PI optimization for unequal-sized particles

Figures 39 and 40 describe the last iteration in the optimization process. The values of optimal design variables were fixed at [23.9700, 33.3005] after exhausting all 15 iterations. The maximum neck size was 16.1905 and Probability of Improvement was 0.4999.

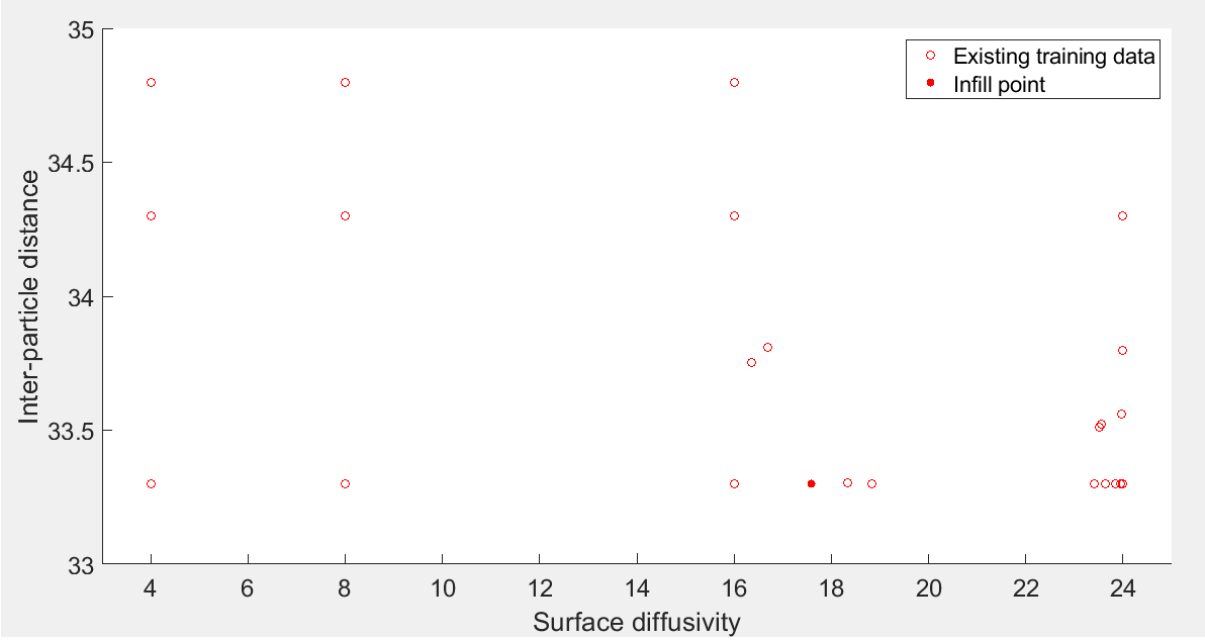

Figure 39: Sampling plan for iteration 15 of PI optimization for unequal-sized particles

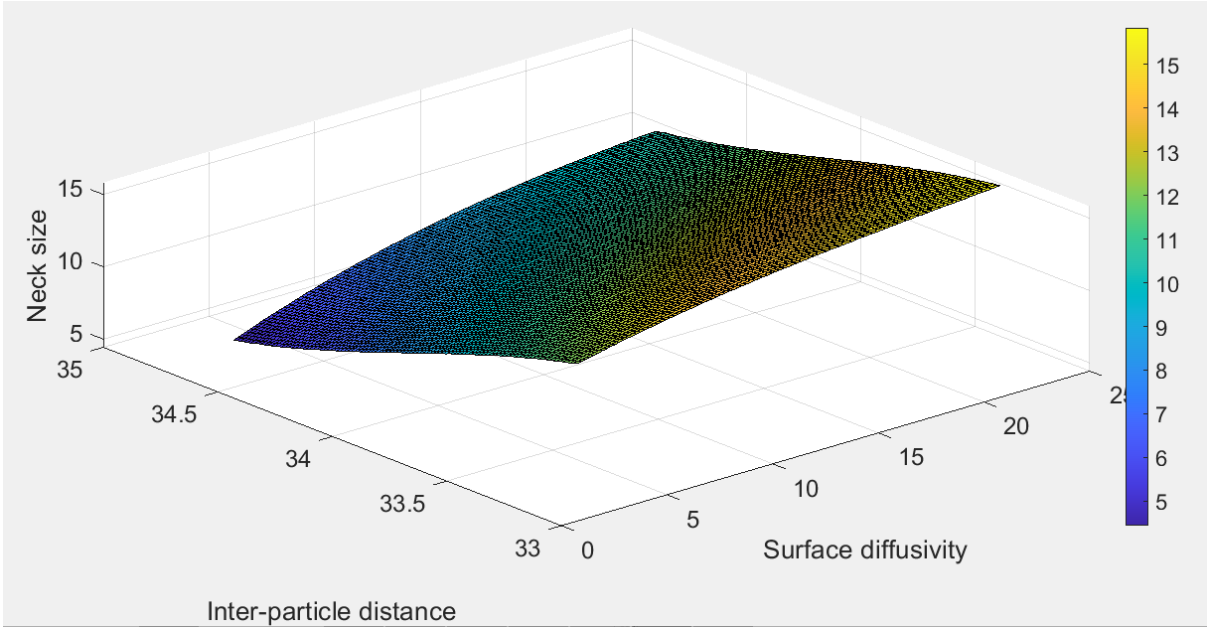

Figure 40: Kriging metamodel after iteration 15 of PI optimization for unequal-sized particles

F. Optimization using Expected Improvement

Figures 41 and 42 show the first iteration of Bayesian Optimization using Expected Improvement (EI) as the acquisition function. Figure 41 displays the input sampling plan with surface diffusivity ranging from 4 to 24 and inter-particle distance from 33.3 to 34.8. Figure 42 shows the initial metamodel generated by Kriging regression and the increasing nature of the neck size with increasing surface diffusivity and decreasing with inter-particle distance.

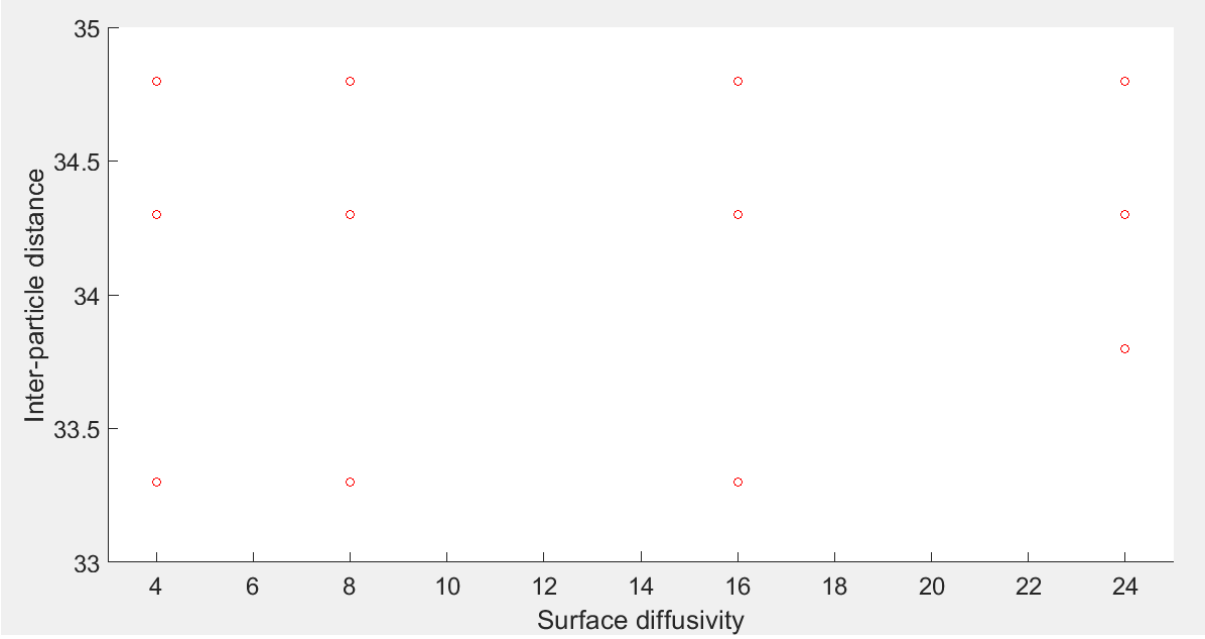

Figure 41: Sampling plan for iteration 1 of EI optimization for unequal-sized particles

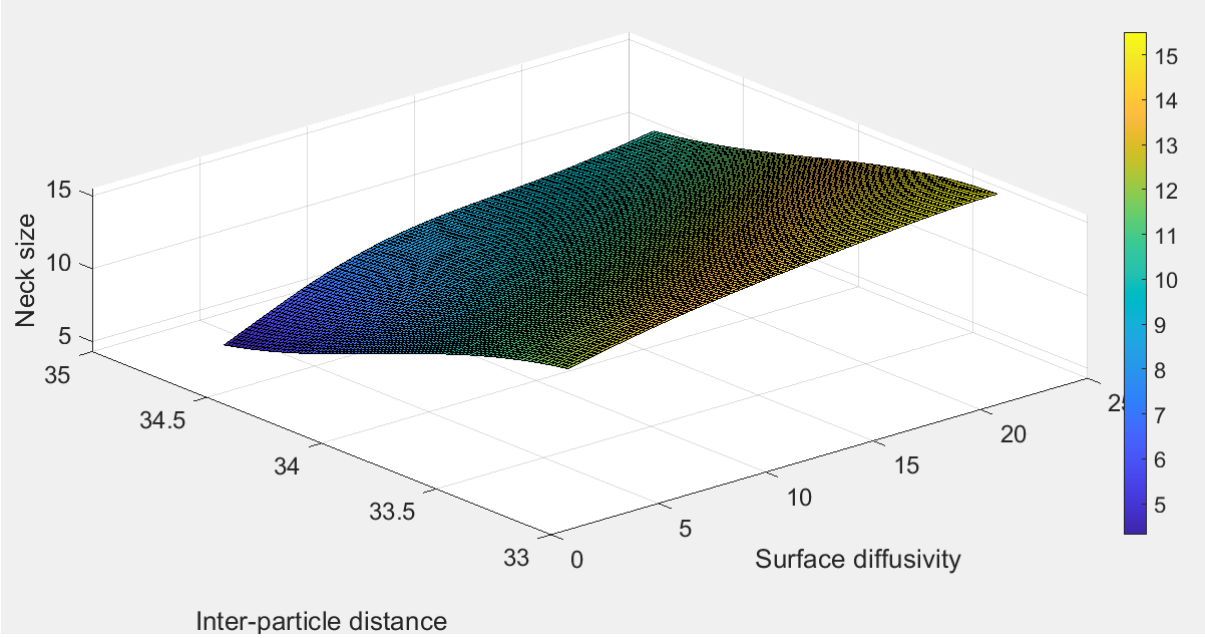

Figure 42: Kriging metamodel for iteration 1 of EI optimization for unequal-sized particles

As shown by figures 43 and 44, at the end of 15 iterations, the values of design variables converged at [23.9893, 33.9627], the maximum neck size being 16.1905 and Expected Improvement as 6.0914e+03. The solution obtained here tends to be a global optimum.

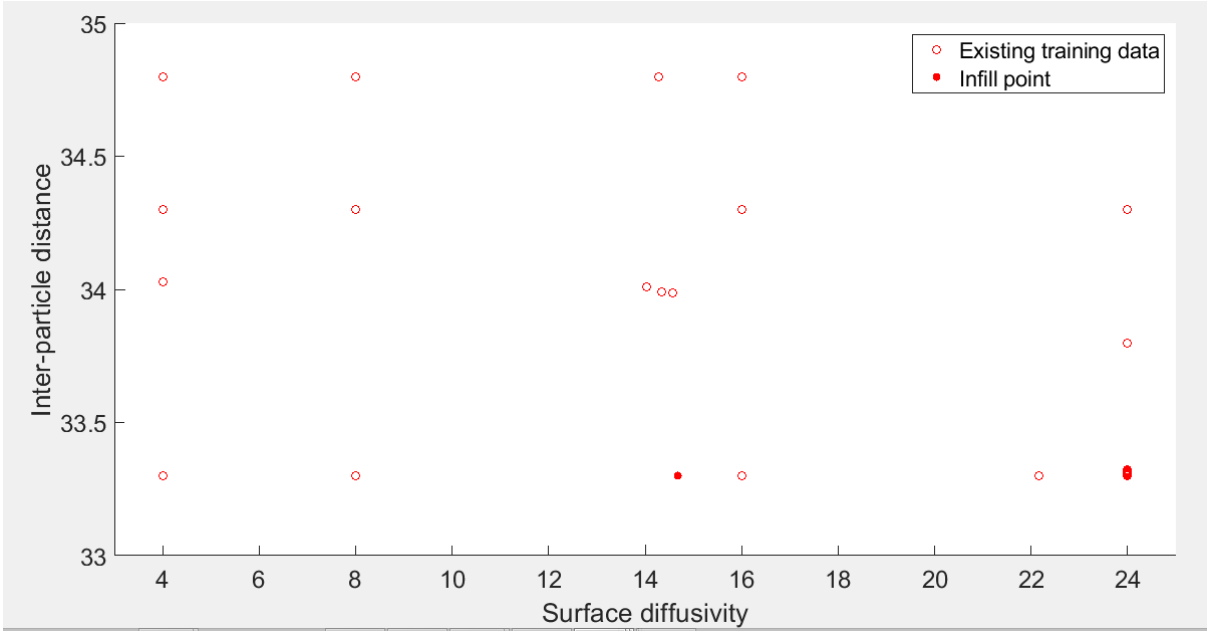

Figure 43: Sampling plan for iteration 15 of EI optimization for unequal-sized particles

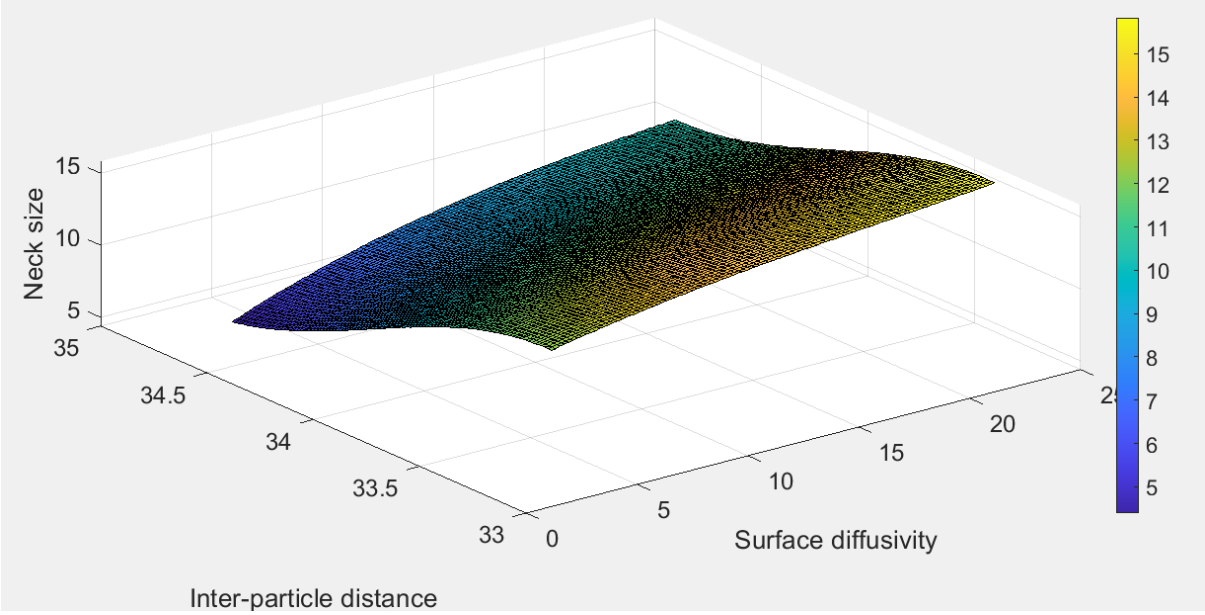

Figure 44: Kriging metamodel after iteration 15 of EI optimization for unequal-sized particles

Figure 45 shows the Probability of Improvement at each iteration for unequal sized particles. Initially, the PI decreases and tends to zero, then becomes constant in the later iterations. The trend is similar to the case for equal-sized particles but here the function will apparently require more than 15 iterations to eventually turn zero.

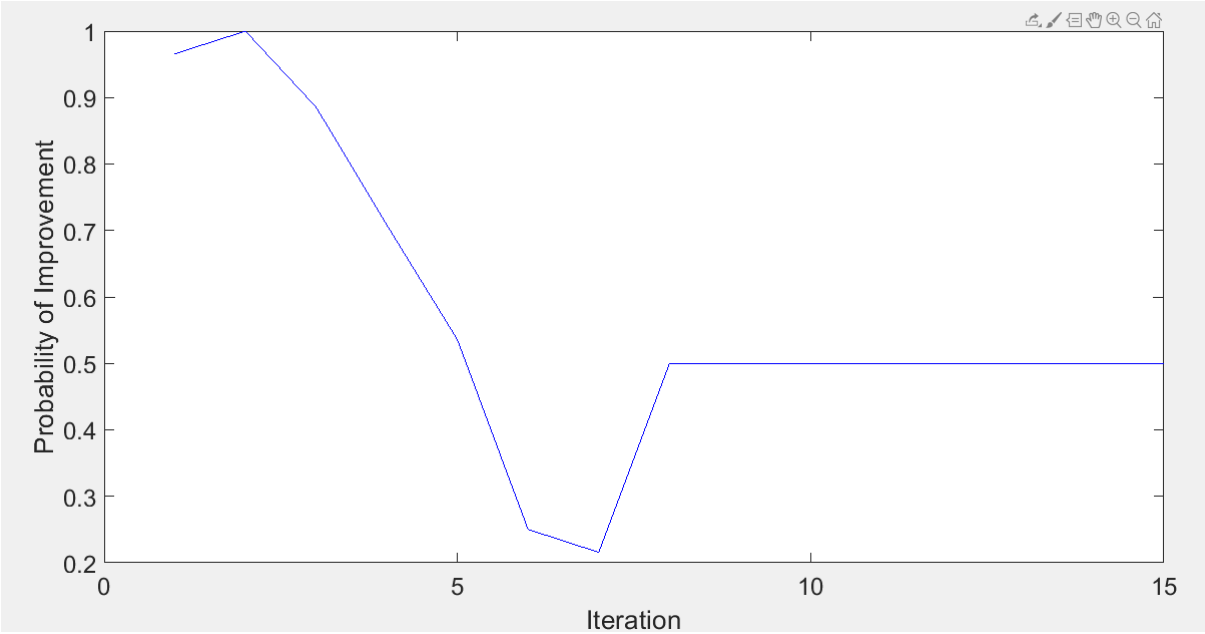

Figure 45: Probability of Improvement at each iteration for unequal sized particles

Figure 46 presents the Expected Improvement at different iterations for unequal sized particles. The EI seems to be higher in the later iterations indicating that the function is trying to improve upon the value of maximum neck size.

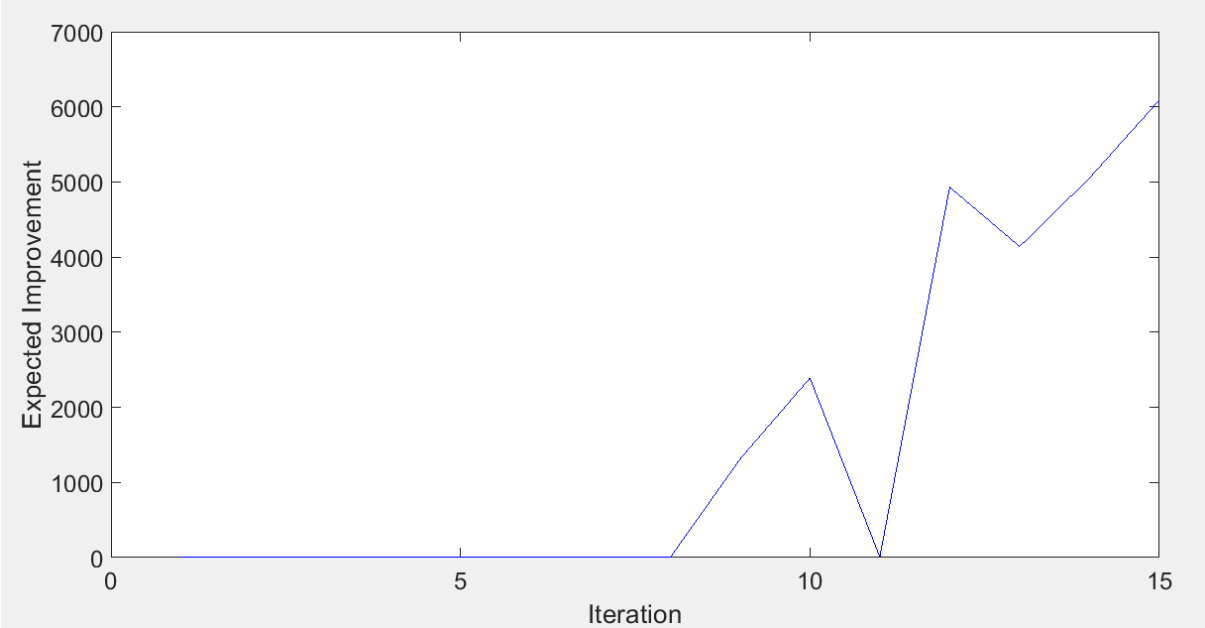

Figure 46: Expected Improvement at each iteration for unequal sized particles

Figures 47 and 48 depict the responses obtained by maximizing the acquisition functions Probability of Improvement and Expected Improvement respectively for unequal sized particles. As in the case of equal-sized particles, there are some high values of neck size which exploit the surrogate while there are some low values of the same which explore the design space. EGO selects designs that lead to maximization of the acquisition function meeting the constraints of input parameters.

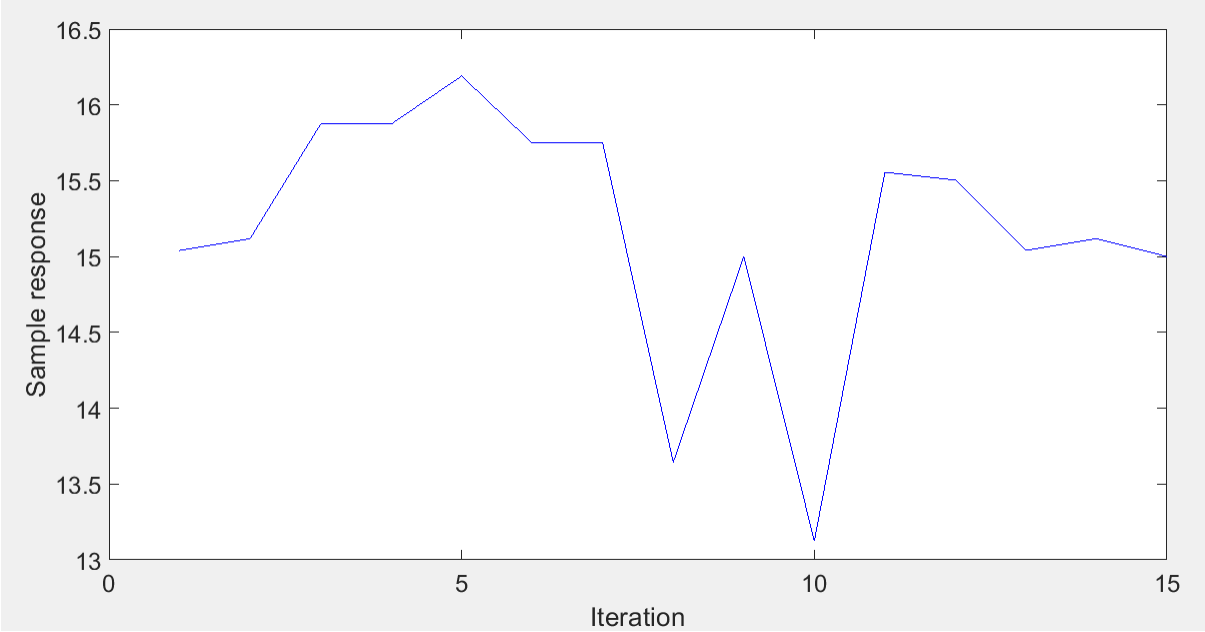

Figure 47: Response of the designs sampled by PI for unequal sized particles

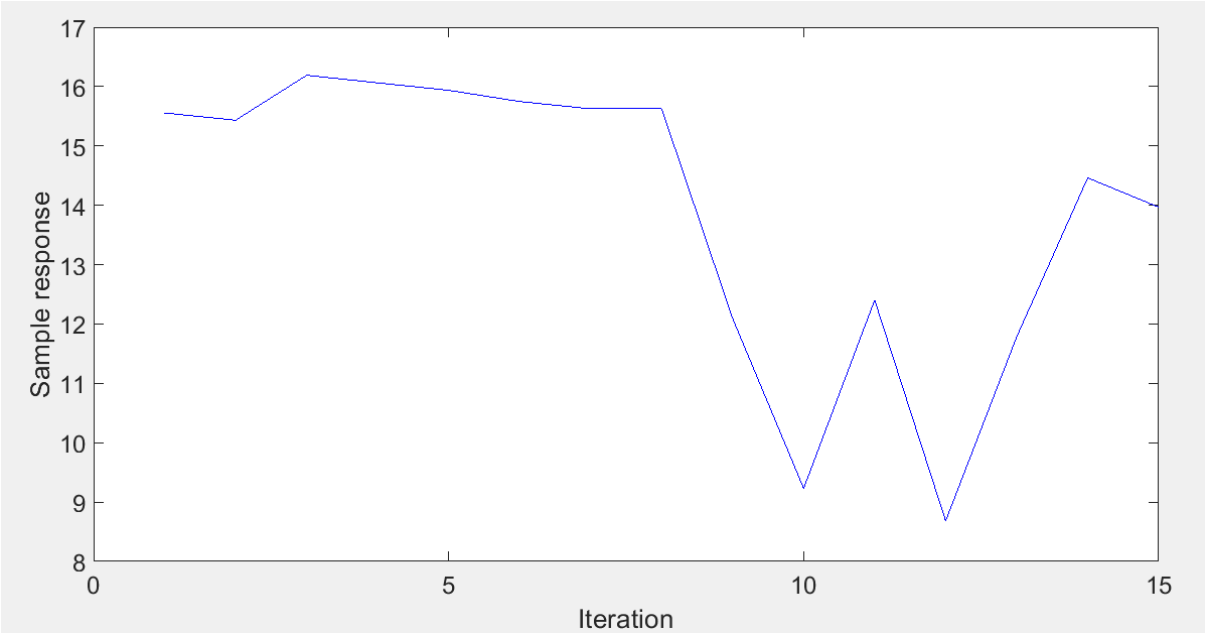

Figure 48: Response of the designs sampled by EI for unequal sized particles

Table 11 lists the optimal values of design variables surface diffusivity D_{surf} and inter-particle distance d as obtained from the two acquisition functions. For equal-sized particles, the Probability of Improvement gives the optimal result as [23.8268, 40.0001] when the design

converged after 10 iterations. The Expected Improvement after 15 iterations provides an optimal design of [23.9874, 40.7428] which indicates a global optimum. For unequal sized particles, the Probability of Improvement provides a solution of [23.9700, 33.3005] while the Expected Improvement provides optimal values of [23.9893, 33.9627] after consuming all 15 iterations.

The maximum value of surface diffusivity present in the sampling plan is 24. The minimum values of inter-particle distance in the sampling plans are 40 and 33.3 for equal-sized and unequal sized particles respectively. Hence, the optimization result validates the theory that surface diffusivity should be as high as possible to have better densification of the material undergoing sintering. The optimal values of inter-particle distance emphasize the fact that lower inter-particle distance leads to a close-packed arrangement of atoms and hence reduction of porosity between the particles. This leads to better mechanical properties of the material. The optimization result from two different acquisition functions looks in good agreement with each other.

Table 11: Optimal values of design variables

Particle size	Optimal design [D_{surf}, d] by Probability of Improvement	Optimal design [D_{surf}, d] by Expected Improvement
Equal	[23.8268, 40.0001]	[23.9874, 40.7428]
Unequal	[23.9700, 33.3005]	[23.9893, 33.9627]

4. CONCLUSION AND FUTURE WORK

Undeniably, sintering is a pervasive material processing technology with its application ranging from laser-based sintering to spark plasma sintering. However, the post-build part quality needs to be focused on for better reliability on this technology and wide usage. In the current work, a machine-learning framework was developed to aid in quality control of the solid-state sintering process. Specifically, the microstructure evolution during the process was optimized. Controlling the microstructure morphology is an essential part of any manufacturing process. Machine Learning has a huge impact on ensuring product quality by predicting the microstructure during the design process.

The process design in the current work was based on two different particle sizes. The following conclusions can be drawn:

- With increasing surface diffusivity, the neck size in between particles always increases irrespective of the particle radii. For equal-sized particles, the neck size increased from 14.15388 to 19.36508 with increase of surface diffusivity from 4 to 24 and inter-particle distance constant at 40. For unequal sized particles, the neck size increased from 12.093 to 15.55554 with the same increase of surface diffusivity and inter-particle distance constant at 33.3. This is because surface diffusivity increases densification in the material and hence enlargement of neck width occurs. The neck size decreases with increase in inter-particle distance independent of particle radii. For equal-sized particles, the neck size decreased from 14.15388 to 5.84617 with increase of inter-particle distance from 40 to 41.5 at constant surface diffusivity of 4. For unequal sized particles, the neck size decreased from 12.093 to 4.30771 for an increase of inter-particle distance from 33.3 to 34.8 with a constant surface diffusivity of 4. This is attributable to the fact that lesser inter-particle distance leads to reduction in porosity and hence better densification due to a close-packed arrangement of particle micro-structure. This helps in enhancing material properties.
- As depicted in section 3.1, shrinkage of particles occurs at an equal rate for equal-sized particles while for unequal sized particles, the smaller particle contracts faster. The neck formation proceeds in the same manner for both equal and unequal sized particles. The

neck sizes for equal-sized particles were 9.02257, 17.36433, 20.96770 and 22.47932 corresponding to time steps 100, 5000, 12,500 and 20,000 while for unequal sized particles the corresponding neck sizes were 8.18180, 14.80311, 16.82539 and 18.66670 for the same time steps. The neck evolution is rapid initially and then slows down later.

- The neck size seems to be higher for equal-sized particles than that for unequal sized particles for the same time steps as illustrated by the phase-field simulation results in section 3.1. This might be due to the rapid shrinkage of the smaller particle in the case of unequal sized particles. Also, Figure 14 shows that the particle size does not have a significant effect on the evolution of neck size during the later stages of sintering process.
- The inter-particle distance has a higher contribution to the variation of neck size than that of surface diffusivity irrespective of particle size. This is evident from the sensitivity analysis results in section 3.2. For equal-sized particles, the value of the correlation coefficient between surface diffusivity and neck size is 0.5733 which indicates a strong positive correlation. The same conclusion can be drawn from the value for unequal sized particles which is 0.5734. The correlation coefficients between inter-particle distance and neck size for equal and unequal sized particles are -0.8028 and -0.7960 respectively which indicate a strong negative association of inter-particle distance with neck size. As the values are closer to -1, the lesser the inter-particle distance, the more the value of neck size should be. Hence, to get better mechanical properties of the material, it is recommended to have the inter-particle distance as small as possible and surface diffusivity as high as possible.
- For both equal-sized and unequal sized particles, the metamodel with regression function of order zero (Regpoly0) is the best initial metamodel. According to Tables 7 and 8, the root mean square error and cross-validation error for Regpoly0 for equal-sized particles are 1.2077 and 0.25836. The same for unequal sized particles are 0.4111 and 0.3149 as inferred from Tables 9 and 10.
- For equal-sized particles, the Probability of Improvement gave optimal values of design variables surface diffusivity and inter-particle distance as 23.8268 and 40.0001 while Expected Improvement provided values 23.9874 and 40.7428 respectively. For unequal sized particles, the optimal design values from Probability of Improvement were 23.9700 and 33.3005 while those from Expected Improvement were 23.9893 and 33.9627. Hence,

the optimization results from the two different acquisition functions tend to concur with each other.

- The optimal values of input parameters surface diffusivity and inter-particle distance validate the general theory that surface diffusivity is preferred to be higher for enhanced densification of the material after sintering while inter-particle distance is desired to be lower for a close-packed arrangement of atoms to reduce porosity and hence increase density of the material.

Future work in this context can include the following:

- Using all 16 training data points to build better surrogate models with lesser root mean square error. If 16 data points are not enough for building the surrogate model, an adaptive sampling approach can be used which will balance the local exploitation and global exploration via an error information. This strategy consists of sequentially selecting new points by maximizing an expected prediction error criterion that considers both the bias and variance information [43], thus making up for data deficit.
- Developing machine-learning methodologies for automatic measurement of neck size.
- Since the trend in the data for neck size is monotonic with respect to the input parameters, the surrogate models can be built using the polynomial response surface method. This can be achieved by the curve fitting toolbox in MATLAB.
- The phase-field simulations can be performed on parallel processors to reduce the time for generating the microstructures.
- Active Learning methodologies can be used to incorporate all essential input parameters to build the metamodels so that the surrogate model covers all the design variables.
- Meta-heuristics techniques may be used to decide the optimal particle size for better mechanical properties of the material.

5. MAJOR CONTRIBUTION

The following were the major activities carried out in this work:

- Performed sensitivity analysis and found the correlation of input parameters surface diffusivity and inter-particle distance with neck size for equal-sized and unequal sized particles during sintering.
- Applied Gaussian Process Regression algorithm to create surrogate models of neck size for equal-sized and unequal sized particles.
- Performed model testing on the surrogate models to quantify root mean square error (RMSE) for the initial metamodels.
- Applied leave-one-out cross-validation algorithm to calculate average error in the initial metamodels.
- Using Bayesian Optimization method, the optimal values of surface diffusivity and inter-particle distance were determined for both equal-sized and unequal sized particles.
- A comparative study was done for optimization by two different acquisition functions, Probability of Improvement and Expected Improvement.

6. REFERENCES

1. Wang, Y.U., *Computer modeling and simulation of solid-state sintering: A phase field approach.* Acta materialia 2006. **54**(4): p. 953-961.

2. German, R.M., in *Metal Additive Manufacturing*. 2019. p. 127-139.

3. German, R.M. *Strength evolution in debinding and sintering*. in *Proceedings of the 3rd International Conference on the Science, Technology & Applications of Sintering*. 2003.

4. Pavan, M., et al., *CT-based quality control of Laser Sintering of Polymers.* Case studies in nondestructive testing and evaluation 2016. **6**: p. 62-68.

5. Dotchev, K. and W. Yusoff, *Recycling of polyamide 12 based powders in the laser sintering process.* Rapid Prototyping Journal 2009.

6. Karapatis, N., et al. *Optimization of powder layer density in selective laser sintering*. in *1999 International Solid Freeform Fabrication Symposium*. 1999.

7. Yamazaki, K., et al., *PAS (plasma activated sintering): transient sintering process control for rapid consolidation of powders.* Journal of materials processing technology 1996. **56**(1-4): p. 955-965.

8. Zarringhalam, H., C. Majewski, and N. Hopkinson, *Degree of particle melt in Nylon-12 selective laser-sintered parts.* Rapid Prototyping Journal 2009.

9. Phillips, T., S. Fish, and J. Beaman, *Development of an automated laser control system for improving temperature uniformity and controlling component strength in selective laser sintering.* Additive Manufacturing 2018. **24**: p. 316-322.

10. Kuang, X., G. Carotenuto, and L. Nicolais, *A review of ceramic sintering and suggestions on reducing sintering temperatures.* Advanced Performance Materials 1997. **4**(3): p. 257-274.

11. Simchi, A. and H. Danninger, *Electrical conductivity and microstructure of sintered ferrous materials: sintered iron.* Powder metallurgy 2000. **43**(3): p. 209-218.

12. Wegner, A. and G. Witt. *Process monitoring in laser sintering using thermal imaging*. in *SFF Symposium, Austin, Texas, USA*. 2011.

13. Olakanmi, E.O., *Effect of mixing time on the bed density, and microstructure of selective laser sintered (sls) aluminium powders.* Materials Research 2012. **15**(2): p. 167-176.

14. Olakanmi, E., R. Cochrane, and K. Dalgarno, *Densification mechanism and microstructural evolution in selective laser sintering of Al–12Si powders.* Journal of Materials Processing Technology 2011. **211**(1): p. 113-121.

15. Zhang, M., et al., *Densification mechanisms and microstructural evolution during spark plasma sintering of boron carbide powders.* Ceramics International 2018. **44**(4): p. 3571-3579.

16. Chen, J., et al., *Study on powder preparation of IGZO target and its effect on sintering.* Journal of Alloys and Compounds 2019. **800**: p. 468-477.

17. Zhang, L., et al., *Low temperature-sintering and microstructure of highly transparent yttria ceramics.* Journal of Alloys and Compounds, 2017. **695**: p. 2580-2586.

18. Dong, C., et al., *Microstructural evolution and sintering kinetics during spark plasma sintering of pure tantalum powder.* Journal of Alloys and Compounds 2019. **781**: p. 84-92.

19. Biswas, S., et al., *A study of the evolution of microstructure and consolidation kinetics during sintering using a phase field modeling based approach.* Extreme Mechanics Letters, 2016. **7**: p. 78-89.

20. Hötzer, J., et al., *Phase-field simulation of solid state sintering.* Acta Materialia, 2019. **164**: p. 184-195.

21. Biswas, S., D. Schwen, and V. Tomar, *Implementation of a phase field model for simulating evolution of two powder particles representing microstructural changes during sintering.* Journal of materials science, 2018. **53**(8): p. 5799-5825.

22. Asp, K. and J. Ågren, *Phase-field simulation of sintering and related phenomena–A vacancy diffusion approach.* Acta materialia, 2006. **54**(5): p. 1241-1248.

23. Kumar, V., Z. Fang, and P. Fife, *Phase field simulations of grain growth during sintering of two unequal-sized particles.* Materials Science and Engineering: A 2010. **528**(1): p. 254-259.

24. Dzepina, B., D. Balint, and D. Dini, *A phase field model of pressure-assisted sintering.* Journal of the European Ceramic Society, 2019. **39**(2-3): p. 173-182.

25. Termuhlen, R., et al., *Three-dimensional phase field sintering simulations accounting for the rigid-body motion of individual grains.* Computational Materials Science, 2020. **186**: p. 109963.

26. LeCun, Y., Y. Bengio, and G. Hinton, *Deep learning.* nature, 2015. **521**(7553): p. 436-444.

27. Swaroop, A., V. Himasree, and T. Thomas, *Machine learning based a priori prediction on powder samples of sintering-driven abnormal grain growth.* Computational Materials Science. **187**: p. 110117.

28. Song, L., et al., *Synthetically predicting the quality index of sinter using machine learning model.* Ironmaking and Steelmaking, 2019: p. 1-9.

29. Xiao, L., M. Lu, and H. Huang, *Detection of powder bed defects in selective laser sintering using convolutional neural network.* The International Journal of Advanced Manufacturing Technology, 2020: p. 1-12.

30. Liu, Q., et al., *Machine-learning assisted laser powder bed fusion process optimization for AlSi10Mg: New microstructure description indices and fracture mechanisms.* Acta Materialia, 2020.

31. Zhouzhi, W., et al., *Transfer learning aid the prediction of sintering densification.* Ceramics International, 2020. **46**(16): p. 25200-25210.

32. Zhang, J.-h., A.-g. Xie, and F.-m. Shen, *Multi-objective optimization and analysis model of sintering process based on BP neural network.* Journal of Iron and Steel Research, International 2007. **14**(2): p. 1-5.

33. Biner, S.B., *Programming phase-field modeling*. 2017: Springer.

34. Rasmussen, C.E. *Gaussian processes in machine learning*. in *Summer School on Machine Learning*. 2003. Springer.

35. Forrester, A., A. Sobester, and A. Keane, *Engineering design via surrogate modelling: a practical guide*. 2008: John Wiley & Sons.

36. Anderson, M.J. and P.J. Whitcomb, *Design of experiments.* Kirk-Othmer Encyclopedia of Chemical Technology, 2000: p. 1-22.

37. Couckuyt, I., T. Dhaene, and P. Demeester, *ooDACE toolbox: a flexible object-oriented Kriging implementation.* Journal of Machine Learning Research, 2014. **15**: p. 3183-3186.

38. Friedman, J., T. Hastie, and R. Tibshirani, *The elements of statistical learning*. Vol. 1. 2001: Springer series in statistics New York.

39. Saltelli, A., et al., *Global sensitivity analysis: the primer*. 2008: John Wiley & Sons.

40. Ghosh, S., et al., *Uncertainty analysis of microsegregation during laser powder bed fusion.* Modelling and Simulation in Materials Science and Engineering 2019. **27**(3): p. 034002.

41. Jones, D.R., M. Schonlau, and W.J. Welch, *Efficient global optimization of expensive black-box functions.* Journal of Global optimization, 1998. **13**(4): p. 455-492.

42. Whitley, D., *A genetic algorithm tutorial.* Statistics and Computing, 1994. **4**(2): p. 65-85.

43. Liu, H., J. Cai, and Y.-S. Ong, *An adaptive sampling approach for Kriging metamodeling by maximizing expected prediction error.* Computers & Chemical Engineering, 2017. **106**: p. 171-182.

7. LIST OF PRESENTATIONS

- Arunabha Batabyal, Jing Zhang, *Uncertainty Quantification of Molecular Dynamics Model for Laser Powder Bed Fusion Process*, 2nd Annual ASM Indianapolis Chapter Spring Conference, February 11, 2020, Purdue University, West Lafayette, Indiana, USA.

- Arunabha Batabyal, Jing Zhang, *Evaluation of Mechanical Properties of Glass Fiber and Carbon Fiber Reinforced Polymer Composite*, ASM Indianapolis Chapter Spring Conference, February 12, 2019, Irwin Conference Center, Columbus, Indiana, USA.